

Analysis of a Mesoscale Infiltration and Water Seepage Test in Unsaturated Fractured Rock: Fracture-Informed Spatial Variability

Quanlin Zhou (QLZhou@lbl.gov) (correspondence author)

Rohit Salve (R_Salve@lbl.gov)

Hui-Hai Liu (HHliu@lbl.gov)

Joseph S. Y. Wang (JSWang@lbl.gov)

Earth Sciences Division, Lawrence Berkeley National Laboratory, University of
California, Berkeley, CA 94720

and

David Hudson (dhudson@usgs.gov)

U.S. Geological Survey, Las Vegas, NV 89144

Abstract

A mesoscale (21 m in thickness) infiltration and seepage test was conducted recently in a deep, unsaturated fractured rock system at the crossover point of two underground tunnels. Water was injected into an infiltration plot of 3 m × 4 m on the floor of an alcove in the upper tunnel, and seepage was collected on the ceiling of a niche of the lower tunnel. Significant temporal and (particularly) spatial variabilities were observed in both measured infiltration and seepage rates. In this study, a modeling analysis was performed to improve understanding of test results and to evaluate the continuum approach for modeling the mesoscale system. A three-dimensional unsaturated flow model was developed, and a column-based heterogeneity method was used to capture heterogeneous hydraulic properties reflected by the observed spatial variabilities. Fracture permeability and a van Genuchten parameter (van Genuchten, 1980) were calibrated for each rock column in the upper and lower hydrogeologic units in the test bed. A strong correlation was found between calibrated fracture properties and measured infiltration/seepage rates, and good matches were achieved between simulated and measured seepage rates. Both these findings demonstrate that the numerical model based on the continuum approach and column-based heterogeneity generally captures the measured seepage processes through a discrete fracture network. The calibrated properties and measured infiltration/seepage rates are further compared with mapped fracture patterns. For the upper unit, good mutual correlations were obtained for calibrated fracture permeability, measured infiltration rates, and density of fractures mapped on the infiltration plot. However, for the lower unit, no correlation could be established between calibrated fracture properties (or measured seepage rates) and density of fractures mapped on the niche ceiling. This lack of correlation indicates the complexity of unsaturated flow within the discrete fracture network, which may be caused by flow focusing/fragmentation and diversion/convergence through these two units, and by water diversion around the niche resulting from capillarity, small fractures, and film flow on the niche ceiling.

Keyword: Unsaturated Flow; Fractured Rock; Numerical Modeling; Heterogeneity; Infiltration; Field Test

1. Introduction

Unsaturated flow in fractured rock has gained increasing attention in the past two decades, particularly in its application to geologic disposal of nuclear wastes and environmental contamination in arid and semi-arid regions (Bodvarsson and Tsang, 1999; Pruess, 1999; NRC, 2001). Unsaturated flow involves many complex physical and dynamic processes (e.g., Glass et al., 1995; Bodvarsson et al., 2003). This complexity results from heterogeneity within single fractures and through fracture networks, nonlinearity in capillarity and relative permeability, fracture-matrix interactions, and contrast in hydraulic properties between fractures and the matrix (Zhou et al., 2003). Moreover, the importance of physical processes is different at different scales of interest: At a large scale, preferential flow along faults and large connected fractures has been recognized as an important feature of water percolation. Evidence of large-scale preferential flow has been collected using environmental isotopes and applied tracers (Liu et al., 1995; Nativ et al., 1995; Fabryka-Martin et al., 1996; Yang et al., 1996). This preferential flow reduces the effective fracture-matrix interface area for flow and transport interaction, and enhances relative permeability for actively participating fractures. In a recent study, an active fracture model was developed to incorporate large-scale preferential flow into continuum approach models (Liu et al., 1998, 2003a). Because of its complexity, the understanding of unsaturated flow in fractured rock, from small-scale mechanisms to large-scale processes, is still evolving (Tokunaga and Wan, 1997; Glass et al., 2002).

Our understanding of unsaturated flow has been improved by laboratory and field experiments for single fractures and small-scale fracture networks. A number of studies have noted that water flow within single fractures exhibits complicated physical processes and dynamic behavior, such as gravity-driven fingers, fragmented flow, flow diversion, and intermittent pulsations (e.g., Nicholl et al., 1994; Brown et al., 1998; Dahan et al., 1999; Su et al., 1999; Salve et al., 2004). Fingers were caused by the in-fracture-plane heterogeneity of fracture apertures, as found by many numerical simulations using spatially varying fracture aperture distributions (e.g., Bear et al., 1993). Recent field experiments conducted in a single fracture (Dahan et al., 1999) and a fault (Salve et al., 2004) demonstrated that flow follows complicated patterns, with strong

spatial variability in infiltration and seepage rates. In fracture networks at a small scale (say, meters), individual fractures and fracture intersections act as capillary barriers or flow integrators at different locations and times. Glass et al. (2002) conducted a field experiment by infiltrating dyed water, under ponding conditions, into a well-connected fracture network. During the excavation of the rock mass to a depth of 5 m, they mapped the fracture network and tracer distribution (the structure of the liquid phase) within a number of horizontal pavements immediately below the infiltration surface. They found that with increasing depth, flow transitioned from pervasive patterns of viscous-force-dominated flow, to unsaturated flow with complex phase structures, such as fragmentation, preferential flow, fingers, irregular wetting patterns, and varied behavior at fracture intersections.

Mesoscale experiments (say, tens of meters) can improve our understanding of physical processes and dynamic behavior at a scale important for many practical applications, including nuclear waste disposal and contamination remediation, because the mesoscale tests are closer to large-scale flow processes (say, hundreds to thousands of meters) in site characterization. To our knowledge, only a few mesoscale field experiments have been conducted for unsaturated flow in fractured rocks (e.g., Faybishenko et al., 2000). These include an infiltration test conducted on a plot of about 80 m² on a sloping surface with controlled rates, with seepage collected in a niche about 30 m below the infiltration plot over soil surface (BSC, 2003a; Liu et al., 2003b). Recently, a field infiltration and seepage test was conducted for a 21-m-thick unsaturated fractured rock, with special attention to spatial variabilities in infiltration/seepage rates measured for a number of infiltration subplots and seepage collection locations. The test provided a unique opportunity to study the relationships between the fracture pattern and the hydrologic response to the infiltration and to evaluate the continuum approach and its ability to capture both small-scale features of unsaturated flow and transitions to more directly relevant mesoscale behavior.

The results of many field tests have been analyzed using numerical modeling. The modeling analysis is usually conducted using either the discrete fracture network (DFN) model (e.g., Cacas et al., 1990; Dverstorp et al., 1992; Therrien and Sudicky, 1996; Ohman and Niemi, 2003) or the continuum approach (Warren and Root, 1963),

depending on test scale and available information on discrete fractures. For analyzing a small-scale test, with discrete fracture patterns available on top and bottom boundaries, the DFN model with explicit discrete fractures embedded within the matrix block can be developed by projecting fractures between the two boundaries (Doughty, 2000; Doughty et al., 2002). For a mesoscale test, such a projection may lead to large uncertainties, and a stochastic generation may thus be needed. However, the DFN model with stochastically generated fracture patterns may not predict both integrated and localized responses, and thus may not illustrate flow and transport processes investigated by field tests. Another concern about applying the DFN model to a mesoscale test is the computational burden: the geometry and hydraulic properties of each fracture need be specified explicitly. Alternative to the DFN model is the continuum approach, which is often used in modeling flow in fractured rock observed in field tests (Finsterle, 2000). However, most previous modeling focused on the integrated response of unsaturated flow to system input (infiltration), neglecting the spatial variability in observed flow rates (e.g., Liu et al., 2003b). Furthermore, calibrated rock properties used in the continuum approach have not been correlated to discrete fracture patterns, thereby neglecting the critical role of individual fractures in conducting water flow, which in the case of geologic disposal of nuclear waste, controls radionuclide migration and contaminant transport.

The objective of this paper is to (1) analyze the infiltration and seepage results of the mesoscale test conducted in the 21-m-thick unsaturated fractured rock, using a numerical model based on the continuum approach, and (2) capture the spatial variability in the measured infiltration and seepage rates by calibrating this model with a column-based heterogeneity method. The fracture maps on the top and bottom boundary of the test bed, and air-permeability data measured through a number of boreholes drilled into the test system, were also used to constrain the model. Whether the calibrated rock properties represent mapped discrete fractures or actively-water-conducting fractures was investigated by analyzing the correlation between calibrated rock properties and the measured infiltration/seepage rates (as well as the discrete fracture patterns). In addition, the role of discrete fractures in conducting water flow was explored by analyzing the correlation between measured infiltration/seepage (representative of complicated discrete

fracture network and dynamic behavior) and discrete fractures mapped on the top and bottom boundaries.

2. Field Testing

The mesoscale infiltration and seepage test evaluated in this study was conducted in the deep, unsaturated fractured rock at Yucca Mountain, Nevada, from August 20, 2002 to March 24, 2003. The detailed description of the test setup and results will be given by Salve et al. (the manuscript is being prepared). For clarity and completeness, a brief description of the test is provided here.

Water was injected into an infiltration plot on the floor of an alcove (Alcove 8) excavated on the south side of the Cross Drift of the Enhanced Characterization of Repository Block (ECRB) (see Figure 1). Seepage was collected on the ceiling of a niche (Niche 3) that was excavated into the wall of the Main Drift of the Exploratory Studies Facility (ESF) and located directly under the infiltration plot. The test consisted of three distinct components for investigating the flow processes: (1) controlled release of water into infiltration subplots on the alcove floor, (2) collection of seepage from the niche ceiling, and (3) borehole monitoring of changes in fracture saturation and water potential.

2.1. Geologic Settings

The ESF Main Drift, a 7.8 km long, 7.6 m diameter tunnel, and the ECRB Cross Drift, a 2.7 km long, 5.0 m diameter tunnel, provide underground access to the hydrogeologic units of welded tuff at the horizon of the proposed repository for nuclear waste disposal at Yucca Mountain, Nevada (Bodvarsson et al., 2003). Niche 3, located at the crossover point of the two drifts, is a small drift approximately 4 m in width and 6.3 m in length. The total surface area of the niche ceiling is 16.4 m². Alcove 8 is wider and longer than Niche 3, covering the entire area of the niche ceiling. The distance from the alcove floor to the niche ceiling is 21 m. The test system is approximately 250 m below the ground surface.

Niche 3 is located within the middle nonlithophysal unit (Tptpmn) of the Topopah Spring welded tuff (TSw), a single cooling unit that formed about 12.8 Ma when a thick pyroclastic flow erupted from its volcanic sources (Buesch and Spengler, 1998). The

Tptpmn unit is a densely welded, highly fractured devitrified zone, containing few lithophysal cavities. Alcove 8 is situated within the upper lithophysal (Ttpul) unit of the TSw unit. The Ttpul contains large, naturally occurring cavities (called lithophysae) attributed to gas and vapor-phase constituents entrapped and redistributed during the initial deposition, compaction, and gas migration out of the TSw unit. The majority of fractures appear to be cooling features associated with lithophysae cavities. Cavities and fractures in the Ttpul unit lead to large effective fracture porosity. The calibrated porosity in a fault test conducted in the same system is 6.6%, which is much larger than the effective porosity (1%) of the Tptpmn unit (Liu et al., 2004). The contact interface between these two hydrogeologic units is nearly horizontal, approximately 14.5 m below the alcove floor.

The two hydrogeologic units exhibit different fracture geometric characteristics obtained from Full-Periphery Geologic Maps (FPGMs) and the Detailed Line Survey (DLS) of the Main Drift and the Cross Drift (Hinds et al., 2003). Within the Ttpul unit (henceforth referred to here as the “upper unit”), fracture frequency varies significantly, with a mean value and a standard deviation of $0.8 \pm 1.0 \text{ m}^{-1}$ (BSC, 2003c). The fracture trace length (L_f) is also highly variable, ranging from 1.0 m to 29 m, with $\log(L_f) = 0.41 \pm 0.33$. Variability in fracture frequency and trace length was also obtained within the Tptpmn unit (henceforth referred to here as the “lower unit”), where about 10,000 fractures were sampled. The mean and standard deviation of fracture frequency are $4.3 \pm 3.4 \text{ m}^{-1}$, while the values for fracture trace length (ranging from 1.0 m to 70 m) are $\log(L_f) = 0.33 \pm 0.29$. Note that the fracture trace length was calculated using fractures longer than 1.0 m. Smaller fractures (i.e., still longer than 0.3 m but less than 1.0 m) were mapped, but only within a 3 km segment (out of the total tunnel of 7.8 km) of the Main Drift (not part of the test location). The trace-length distribution of all surveyed fractures for this segment showed that the fracture trace length varies from 0.3 m to 10.0 m (Hinds et al., 2003, Figure 5). Matrix characteristics are fairly homogeneous within these two units (Flint, 1998a, b). The mean matrix permeability values for laboratory rock cores are nearly five orders of magnitude less than mean fracture permeability values in these two hydrogeologic units.

2.2. Infiltration Test

A plot of $3\text{ m} \times 4\text{ m}$ was trenched as an infiltration area on the floor of Alcove 8 (see Figure 2). The plot was divided into 12 separated subplots, each of which had the same area, $1\text{ m} \times 1\text{ m}$. Each subplot was connected to a permeameter through which water was applied. The water level in each subplot was maintained at a head of 2 cm. It was assumed that the flux for applied water from the permeameter was identical to the infiltration rate into the fractured rock, except on the first day, when the water storage of 20 L used for the 2 cm water level was excluded. The infiltration plot was covered with a tarp to minimize the loss of water from evaporation along the infiltration zone.

Figure 3 shows the (time) series of the total infiltration rates, exhibiting a three-stage pattern. The total infiltration rate at a given time is defined by the overall infiltration rate through the entire plot. The infiltration rate was very high on the first day, reaching a value of 644 L/day, excluding the water storage for the 2 cm water head. The total rate decreased sharply over the following five days (the first stage) and reached 61 L/day on the 5th day. In the second stage, the rate increased steadily to a value of 334 L/day by the 29th day. Once the infiltration rate reached its second peak value, the rate decreased in the third stage (from the 29th day to 215th day). In the third stage, the infiltration rate decreased sharply within the first 40 days, at the end of which the rate was 64 L/day. This rate remained relatively stable until the 120th day, when the infiltration rate decreased further to 50 L/day, after which it continued to gradually decline. The maximum infiltration rate on the first day was about 13 times as large as that under quasi-stable conditions after 120 days of liquid release. Superimposed on the main trend of the three-stage infiltration series were high-frequency fluctuations that occurred during the entire infiltration period.

Figure 4 shows the transient infiltration-rate series measured in each of the 12 infiltration subplots. The strong spatial variability of infiltration rates was observed in terms of the magnitude and transient pattern of infiltration rates through different subplots. A number of subplots shared a transient three-stage infiltration pattern similar to the total infiltration rate; the other subplots had a relatively stable infiltration rate through the entire test period. The heterogeneity in fracture permeability (and fracture

density) in the upper unit as demonstrated by the measured infiltration rates was incorporated into the modeling analysis to be discussed in Section 3.

2.3. Seepage Test

Seepage was collected at the ceiling of Niche 3 by a capture system. The capture system consisted of 176 0.3 m × 0.3 m (1 ft by 1 ft) compartments constructed by transparent lexan plastic. The total cross-sectional area of the capture system was 16.4 m², with some space left between compartments for maintenance. These compartments were classified into 11 tray units of different surface areas, based on field characteristics (see Figure 5). An additional collection tray unit was used to collect seepage flowing along the niche's right wall. Water dripping into each of the tray units was collected into a container connected with this tray unit, the container was in turn connected to a pressure transducer used to remotely monitor seepage rates and volume, and the seepage rates (in L/day) were recorded for the container. The seepage rates in different tray units reflected the spatial variability in the seepage on the niche ceiling. To minimize the effects of evaporation resulting from the Main Drift ventilation, the bulkhead door at the entrance to the niche was closed and sealed. The measured humidity was close to 100% during the test period, indicating that evaporation had little effect on water mass balance.

The total seepage rate measured for the 12 tray units is shown in Figure 3, exhibiting strong temporal variability. Seepage occurred 30 days after liquid release. The seepage rate increased rapidly up to 30 L/day within 2–3 days. This high seepage rate remained relatively stable for about 30 days, after which the total seepage rate declined significantly over the following 30 days. The seepage rate decreased further after the 90th day, but the rate of decline decreased.

We define recoverability, for a given time period, by using total average seepage rate observed in Niche 3 as a percentage of the total average infiltration rate through the infiltration plot. About 15% of the infiltrated water seeped out of the fractured rock into the niche at early time (the first 90 days since liquid release). At later time (the last 125 days), recoverability was 10%. In the last 10 days, recoverability dropped further to 8.6%.

Figure 6 shows the time series of seepage rates measured for each of the 12 tray units on the niche ceiling. Note that the seepage rate at a given time (used for a individual tray unit) are normalized to the size of the tray unit by dividing the measured seepage rate for this tray unit by its total number of subtray assemblies. A subtray assembly is of an area 0.3 m by 1.2 m (1 ft by 4 ft).

2.4. Travel-Time Monitoring

Within the fractured rock, changes in saturation (and water potential) were monitored using boreholes drilled around Niche 3. Within each borehole, electrical resistivity probes located at 0.25 m long intervals recorded the electrical resistivity of fracture water over the entire test period. A sharp drop in the electrical resistivity monitored indicates an increase in fracture saturation, which is in turn representative of wetting-front arrival of liquid flow within the fracture network (Salve et al., 2003). The travel time of wetting fronts, measured along three horizontal boreholes approximately 0.5 m above the niche ceiling (see Figure 1), was fairly uniform for the entire ceiling. The travel time from the infiltration plot to the borehole sensors was about 29 days.

3. Modeling Analysis

To understand the test infiltration and seepage rates presented in Section 2, we developed a three-dimensional unsaturated flow model. To match the observed temporal and spatial variabilities, we used a column-based heterogeneity method to represent the spatially varying rock properties. The model was calibrated using the time series of measured infiltration rates in each subplot and of measured seepage rates in each tray unit.

3.1. Governing Equations

The continuum approach was used to simulate unsaturated flow (with strong transient behavior) in fractured rock. This approach has previously been used for modeling unsaturated flow at Yucca Mountain (Doughty, 1999; Wu et al., 1999; Finsterle, 2000; Finsterle et al., 2003; Liu et al., 2003b). Specifically, the multiple interacting continuum (MINC) approach was used to accurately simulate the transient interaction of flow between the matrix and fractures (Pruess and Narasimhan, 1985;

Pruess et al., 1999). Using this approach, fractures are represented by a fracture continuum, while the matrix is represented by a number of nonoverlapping matrix continua, starting from the fracture-matrix interface and extending to the center of a matrix block. The thickness of a matrix gridblock decreases from the central matrix to the fracture-matrix interface, to capture the steep hydraulic gradients of transient flow along the interfaces between fractures and the matrix.

On the scale of an individual gridblock, it was assumed that unsaturated liquid flow can be described using Richards (1931) equation. This equation can be written:

$$\frac{\partial \phi_f S_f}{\partial t} = \frac{\partial}{\partial x_i} \left(\frac{k_f k_{rf}}{\mu} \frac{\partial}{\partial x_i} (P_f + \rho g z) \right) \quad (1)$$

for fracture flow and

$$\frac{\partial \phi_m S_m}{\partial t} = \frac{\partial}{\partial x_i} \left(\frac{k_m k_{rm}}{\mu} \frac{\partial}{\partial x_i} (P_m + \rho g z) \right) \quad (2)$$

for matrix flow, where ϕ is the porosity, S is the liquid saturation, k is the permeability, k_r is the relative permeability, μ is the dynamic viscosity, P is the liquid-phase pressure, ρ is the fluid density, g is the gravitational acceleration, x_i is the Cartesian coordinate, z is the vertical component of x_i , t is the time, and subscripts f and m denote values for the fracture and matrix continua, respectively. In this study, we assumed that the air is passive with a reference pressure, P_{air} , and the liquid-phase pressure for continuum a ($a = f, m$) is related to the capillary pressure, P_c :

$$P_a = P_{air} + P_{ca} . \quad (3)$$

Relative permeability and capillary pressure are functions of liquid saturation as given by van Genuchten (1980):

$$k_{ra} = S_{ea}^{1/2} \left(1 - \left(1 - S_{ea}^{1/m_a} \right)^{m_a} \right)^2, \quad (4)$$

$$P_{ca} = -\frac{1}{\alpha_a} \left(S_{ea}^{-1/m_a} - 1 \right)^{1-m_a}, \quad (5)$$

where the effective saturation S_e is defined as

$$S_{ea} = \frac{S_a - S_{ra}}{1 - S_{ra}}, \quad (6)$$

α and m are two van Genuchten (VG) parameters, and S_r is the residual liquid saturation.

3.2. Column-Based Heterogeneity

To capture the spatial variability in infiltration and seepage rates measured in the test, we used a column-based heterogeneity method in the modeling analysis (Zhou et al., 2004). With this method, a number of rock columns can be selected for each hydrogeologic unit, based on available flow-system data (e.g., flow rates) and measured rock properties. Uniform rock properties within each rock column are assumed, whereas different rock properties may exist between different rock columns. The flow redistributes among different columns within the same hydrogeologic unit, because of lateral differences in rock properties. The introduced deterministic heterogeneity was based on the following three considerations: (1) previous fracture-network modeling has demonstrated that unsaturated flow paths within a fracture network are generally vertical, as a result of gravity-dominated flow (e.g., Liu et al., 2002); (2) the mapped fractures are near-vertical in the study area as well as around the Main Drift and Cross Drift; and (3) not enough fracture data are available to characterize detailed flow paths between Alcove 8 and Niche 3. A simple model of heterogeneity generally involves a relatively small number of parameters to be calibrated.

The number of rock columns within the upper (or lower) unit was determined from available data (for model calibration) on infiltration (or seepage) series. In this test, 12 infiltration subplots with measured infiltration rates were available. As a result, there were 12 rock columns in the upper unit, each of which corresponding to an infiltration subplot. An additional rock column was used for the rock mass surrounding the central 12 columns. The same method was used to define the rock columns in the lower unit. Thus, there were 12 rock columns for the lower unit, each of which corresponded to the configuration of a seepage tray unit. Note that Tray Unit 11, the largest tray unit, was

divided into three parts and regrouped into three rock columns (ranging from 10 to 12), because the same discretization in the x direction (cross Niche 3) was used in the numerical grid for a row of grid blocks in the y direction (along Niche 3) (see Figure 7). An additional rock column was also used for the rock mass surrounding the central 12 rock columns.

For each of the central rock columns, we employed a measured infiltration (or seepage) series for calibrating rock properties within the column. To reduce the number of rock parameters (unknowns for calibration), we considered only the most sensitive parameters to the measured flow rate, while all other rock parameters were assumed to be uniform within a hydrogeologic unit. In this case, fracture permeability (k_f) and fracture van Genuchten alpha (α_f) were the most important rock properties for water flow redistribution, while fracture VG m (m_f) was assumed to be homogeneous within each of the two hydrogeologic units. Uniform permeability and VG parameters were used for the matrix continuum for each hydrogeologic unit, because the correlation length of matrix rock properties was large relative to the test system dimensions at the test site (Zhou et al., 2003).

As a result, two unknowns were to be calibrated for each of the 26 rock columns (13 columns for the upper unit, and 13 columns for the lower unit). For the lower unit, the measured seepage series over 215 days could adequately constrain the two unknowns for each rock column. For the upper unit, however, the infiltration rate for a rock column is sensitive to saturated hydraulic conductivity, but not sensitive to α_f in the rock column. In this case, a uniform α_f was assumed for the central 12 rock columns. We thus had 26 unknowns for the lower unit and 15 unknowns for the upper unit.

3.3. Model Development

A three-dimensional numerical model was developed to simulate the variably saturated flow in fractured rock. The unsaturated flow was simulated using TOUGH2, a numerical simulator for nonisothermal flows of multicomponent, multiphase fluids in one, two, and three-dimensional porous and fractured media (Pruess et al., 1999).

3.3.1. 3-D Mesh

A three-dimensional domain was used for simulations (see Figure 7). The domain was bounded on the top by the floor of Alcove 8, and on the bottom by the floor of Niche 3, with a thickness of approximately 25 m. The niche was located in the center and represented by an opening space. For simplicity, the niche ceiling was approximated by a flat surface 3.2 m above the niche floor. Domain sizes in the horizontal direction were determined from the flow plume observed by radial boreholes drilled around the niche. The domain was 20 m wide and 10 m long along the niche axis. Shown at the top of the grid are the 12 infiltration subplots and the projected boundary of the niche ceiling. The domain contact between the upper and lower units was approximated by a horizontal surface, located at 14.5 m below the alcove floor (top boundary). To capture diverted water flow around the contact interface caused by difference in rock properties, fine vertical discretization was used around the interface. Fine vertical discretization was also used to accurately capture diverted water flow around the niche ceiling caused by capillary barrier effects (Philip, 1990; Finsterle, 2000). In the horizontal plane, a fine grid size was used for the central area of the infiltration and seepage test. Each infiltration subplot covered 2×2 grid blocks, and each rock column in the lower unit covered 1×4 grid blocks. Coarse blocks were used for the zone away from the central area of the test. As discussed above, for each grid block there were one fracture block and five matrix blocks, because the MINC method was used to represent the interaction between fractures and the matrix. In total, there were 67,320 blocks (for fractures and the matrix) and 140,000 connections in the three-dimensional mesh.

3.3.2. Boundary and Initial Conditions

Two possible boundary conditions could be specified at the infiltration plot, because both water head and water flux were quantified from the test. The constant water-pressure head (2 cm) might be specified at the infiltration plot: This condition produced stable infiltration rates over time into the underlying system, because the saturated hydraulic conductivity was assumed to be time-independent. However, the observed infiltration series reflects much more complicated dynamic effects occurring in the unsaturated system; thus, the constant-head condition was not used here. Instead, the measured infiltration rates as a function of time (reflecting the complex dynamic behavior

of the time-dependent saturated hydraulic conductivity for rock immediately beneath the infiltration plot, and the capacity of flow within the water-conducting fracture network) were used as boundary conditions at the infiltration plot. The remaining area on the top boundary was assumed to be impervious, and the side boundaries corresponded to no-flow conditions. The ceiling and sidewall boundary of the niche was modeled by a zero-capillary-pressure condition, representing capillary barrier effects (Finsterle, 2000). The other bottom boundary was assigned by free drainage conditions.

The initial water saturation in the matrix and fracture continua was difficult to ascertain, because the ambient flow conditions were disturbed by a fault test conducted before this test, and by construction water used for the excavation of Alcove 8 (Liu et al., 2004; Salve et al., 2004). Under ambient flow conditions, matrix saturation is 0.72 for the upper unit and 0.85 for the lower unit (Flint, 1998b). The actual matrix saturations were expected to be higher than the ambient values, because of the nearby fault test. In the model analysis, 0.86 and 0.92 were used as the initial matrix saturation values for the upper and lower units, respectively. A high degree of uncertainty may exist in the initial conditions used, but this uncertainty may not have a significant effect on the infiltration and seepage series at the later time of the test. A uniform fracture saturation of 1.05×10^{-2} (for the ambient conditions) was used for both hydrogeologic units, because fractures can drain quickly and recover from previous wetting.

3.3.3. Fracture and Matrix Properties

The fracture characteristics specific to the test site are particularly important to analyzing test results. To accurately characterize the fracture network at the test site, the U.S. Geological Survey (USGS) mapped fractures on the floor of Alcove 8 and the ceiling of Niche 3 (see Figures 2 and 5). Only large natural fractures (longer than 1.0 m) were surveyed; excavation-induced fractures and other small fractures were excluded from the maps. As shown in Figure 2, 24 large fractures can be identified, with two different fracture sets intersecting (almost perpendicularly) with each other in terms of fracture strikes. Most fractures share a similar dip, in a range between 69° and 88° . The fracture frequency calculated based on the map is 1.0 m^{-1} , which is similar to the mean value (0.8 m^{-1}) for the entire upper hydrogeologic unit. Four large fractures pass through

the central area of the niche ceiling along the niche axis at approximately 30°. Intersecting the four fractures, a number of small fractures were also mapped on the ceiling and sidewalls of the niche. The calculated fracture frequency is 1.5 m^{-1} , and fracture spacing is 0.67 m. The fracture frequency calculated for the test site is much less than that for the entire lower unit, indicating that Niche 3 is located in a moderately fractured zone of relatively low fracture density, as shown in the fracture density contour map by Wang and Bodvarsson (2003, Figure 3c). The site-specific fracture frequency was used to calculate the geometric interface area between fracture and matrix continua per unit volume of rock mass.

Fracture air permeability was measured along several horizontal boreholes around Niche 3 under both pre-excavation and post-excavation conditions, and along six near-vertical boreholes around Alcove 8 under post-excavation conditions (Cook, 2000; BSC, 2003a) (see Figure 1). Before niche excavation, seven 9.0 m long horizontal boreholes were drilled into the rock along the niche axis. Along each borehole, air-injection tests were conducted for each packed-off interval of 0.3 m, and air-permeability data were obtained. After excavation, the three boreholes located at approximately 0.5 m above the ceiling were left, and the others were excavated with the rock mass. In addition, seven 6.0 m long radial boreholes were drilled inside the niche. Air permeability was also measured for the three above-niche boreholes and the seven radial boreholes under post-excavation conditions. The fracture permeability varies along boreholes and between different boreholes. The mean and standard deviation of log air permeability for the borehole cluster around Niche 3 are $\log k_f = -13.4 \pm 0.70$ (with permeability unit of m^2) under pre-excavation conditions and -12.4 ± 0.82 under post-excavation conditions. This indicates that the post-excavation air permeability is one order of magnitude higher than the pre-excavation counterpart, because of excavation-induced stress release (Wang and Elsworth, 1999). However, the niche excavation has little effect on the air-permeability profile along each borehole. This can be seen from the similar standard deviation for both conditions. For Alcove 8, the air-permeability data obtained for six (15 m long) near-vertical boreholes produced a mean and standard deviation: $\log k_f = -13.1 \pm 1.29$. The

fracture air permeability data were used for comparison with calibrated fracture permeability values to be discussed in Section 4.

The rock properties of the matrix continuum used in the model are effective porosity (ϕ_m), permeability (k_m), and VG alpha (α_m) and VG m (m_m). Matrix rock properties obtained from the calibration of rock properties for the site characterization of Yucca Mountain were used here (BSC, 2003b), because it is believed that these matrix rock properties are relatively homogeneous for the entire mountain. The calibrated rock properties, in the order ϕ_m , k_m , α_m , and m_m , are 0.15, $3.08 \times 10^{-17} \text{ m}^2$, $2.13 \times 10^{-5} \text{ Pa}^{-1}$, and 0.30 for the upper unit, respectively; and 0.11, $4.07 \times 10^{-18} \text{ m}^2$, $3.86 \times 10^{-5} \text{ Pa}^{-1}$, and 0.29 for the lower unit, respectively. For fracture properties, the calibrated VG m (m_f) value for site characterization was also used in the current model, with a value of 0.61 for both the upper and lower units. However, values of fracture porosity (ϕ_f), k_f , and α_f specific to the test site were used, because of the strong spatial variability in these rock properties. The test-site-specific fracture porosity for both the upper and lower units, calibrated from a fault test near the test site, was used here (Liu et al., 2004); fracture porosity is 6.6% and 1.0% for the upper and lower units, respectively. The remaining two rock properties (k_f and α_f) at the test site were calibrated in the following section.

3.4. Model Calibration

The flow model developed in Section 3.3 was calibrated to match temporal and spatial variabilities in measured infiltration and seepage rates. Through this calibration, site-specific rock properties (and column-specific rock properties for heterogeneity) were obtained. The rock parameters to be calibrated were k_f and α_f for each of the 13 rock columns in the lower unit, k_f for each of the 13 rock columns in the upper unit, and α_f assumed to be common for the central 12 columns and for the rest of the rock-mass column in the upper unit. There were a total of 41 unknowns to be calibrated, 26 parameters for the lower unit and 15 parameters for the upper unit.

The calibration proceeded in stages guided by available information and physical consideration. For the upper unit, the infiltration data in 12 subplots were used to better

constrain the k_f unknowns. For each rock column, the k_f value was determined by matching the maximum measured infiltration rate (excluding the first day) and the simulated infiltration rate. The maximum infiltration rate was considered to be the saturated hydraulic conductivity for the column (Faybishenko et al., 2003). The top boundary condition for flow in this case was the 2 cm water head constant with time. A trial-and-error method was used to reduce the mismatch between the measured maximum infiltration rate and the stable infiltration rate for a given k_f value. The fracture permeability obtained independently for each rock column was further calibrated using a scale factor. The final calibrated $\log k_f$ for a rock column is the calibrated scale factor times the $\log k_f$ obtained by the trial-and-error method. In this way, the effects of observed spatial variability in infiltration rates were generally captured by model calibration, and the number of unknowns to be calibrated reduced to 30. In model calibration, the measured time-dependent infiltration rates were used as the top boundary condition.

The data used for the calibration primarily for the lower unit included the series of measured seepage rates for each of the 12 tray units and the travel time of 29 days measured at a location 0.5 m above the niche ceiling. Because of strong temporal variability in the measured seepage rates, the entire seepage series was divided into three time periods: (1) the first 30 days with no or little seepage, (2) the next 60 days with strongly (temporarily) varying seepage rates, and (3) the last 125 days with quasi-stable seepage rates. The objective function in the model calibration was defined by:

$$obj. = \sum_{j=1}^{13} \left(\sum_{t=1}^{30} \omega_1 (q_{jt}^m - q_{jt}^s)^2 + \sum_{t=31}^{90} \omega_2 (q_{jt}^m - q_{jt}^s)^2 + \sum_{t=91}^{215} \omega_3 (q_{jt}^m - q_{jt}^s)^2 + \sum_{t=1}^{20} \omega_4 (0 - q_{jt}^s)^2 \right) \quad (7)$$

where q_{jt} is the seepage rate at day t (since infiltration started) for the j tray unit ($j = 13$ for the total seepage rate), superscripts m and s denote measured and simulated values, respectively, and ω is the weight factor. The first three terms in Equation (7) represent the misfit between measured and simulated seepage rates, and the last term represents the misfit between measured and simulated travel times. Different values for the weight factor were used for different time periods because different dynamic behavior of the

seepage was observed. For the first term, no or little seepage occurred and a small weight was used; For the second term, the strong temporal variability of seepage rates is an important indicator of the unsaturated system, and the same weight ($\omega_2 = \omega_1$) was used; a value of ω_3 ($= 2\omega_1$) was used to focus on the later, quasi-stable seepage rates because the quasi-stable flow condition will be used for tracer tests. Because it was difficult to introduce the misfit between the simulated and measured travel times of wetting fronts, we used the misfit between the measured and the simulated seepage rates to constrain misfits of the travel times. A higher weight factor ($\omega_4 \approx \omega_3$) was used in the last term in Equation (7) to force seepage not to occur within the first 20 days, while allowing for the occurrence of seepage between the 20th and 30th day because the smaller weight factor (ω_1) was used for this period. The reason for doing this was that many retardation factors (e.g., dynamic connectivity of water-conducting fractures) affecting the wetting-front travel times could not be captured in the current continuum-approach numerical model.

The model calibration reduced the objective function by adjusting the 30 unknowns (parameters for rock properties). Calibration was performed using the inverse modeling code iTOUGH2 (Finsterle, 1999)—the parallel version of iTOUGH2 was used to reduce calibration time, because variably saturated flow over 215 days with strong transient behavior was simulated in each forward run. The calibration time needed for the parallel calibration was a small fraction (approximately 10%) of that needed for non-parallel calibration, making it possible to calibrate the spatial variability of rock properties in a complex unsaturated flow system.

4. Results and Discussion

Calibrated fracture properties in the upper and lower units and a match between simulated and measured seepage rates for each of the 12 central rock columns in the lower unit (as well as match for total seepage rates) are discussed in this section. Correlations of the calibrated rock properties in the upper (or lower) unit with the measured infiltration (or seepage) rates, and density of fractures mapped on the alcove floor (or niche ceiling), are analyzed to explore whether the calibrated rock properties represent mapped discrete fractures or actively-water-conducting fractures, whose

lumped contribution is reflected by the measured infiltration/seepage rates. We are also interested in exploring whether the current numerical model based on the continuum approach is able to represent the spatial variabilities in measured infiltration and seepage rates, and to capture their temporal variabilities resulting from the dynamic behavior of water-conducting fractures.

4.1. Correlations in the Upper Unit

Figure 8 shows the calibrated k_f and α_f values for the 13 rock columns in the upper and lower units. Mutual correlations among the calibrated k_f values in the upper unit, measured infiltration rates, and fracture density on the infiltration plot are discussed. For the correlation analysis, the value of each of these three kinds of variables for an infiltration subplot was considered as an independent sample.

4.1.1. Correlation between Calibrated Permeability and Measured Infiltration Rate

The calibrated k_f values for the 12 central rock columns in the upper unit reflect the spatial variability in the measured infiltration rates over the infiltration plot, because the maximum measured infiltration rates were used for constraining the k_f calibration. The largest k_f of $1.86 \times 10^{-13} \text{ m}^2$ is located in Rock Column 11 (corresponding to Subplot 11), where the maximum measured infiltration rate is 119.7 L/day (see Figure 4). The smallest k_f of $1.31 \times 10^{-14} \text{ m}^2$ is situated in Column 7. The maximum measured infiltration rate for Column 7 is 7.0 L/day, which is 17 times less than that in Subplot 11. The calibrated k_f varies over one order of magnitude in the 12 central rock columns. This spatial variability is within the range of air permeability values measured in six 15 m long near-vertical boreholes drilled around the infiltration plot (see Figure 1). The measured air permeability varies over five orders of magnitude, ranging from 3.60×10^{-15} to $6.25 \times 10^{-9} \text{ m}^2$ (BSC, 2003a). The geometric mean of the calibrated k_f values for the 13 rock columns is $4.90 \times 10^{-14} \text{ m}^2$, slightly lower than that of the measured air permeability ($7.94 \times 10^{-14} \text{ m}^2$). The standard deviation of calibrated $\log k_f$ (0.37) is smaller than the deviation (1.29) for the measured air permeability, indicating

that the spatial variability of permeability decreases with increase in the sampling size (the size for rock columns is much larger than the 0.3 m intervals used for measuring air permeability). This is consistent with theoretic findings on scale-dependent permeability (Neuman, 1994).

Calibrated k_f for Column 13 (for the rock mass surrounding the central rock columns) is $1.20 \times 10^{-12} \text{ m}^2$, one order of magnitude larger than the largest k_f in the central rock columns. Such a difference in the calibrated k_f may result from the inability of the current numerical model to capture flow diversion caused by non-vertical fractures. In such non-vertical fractures, water flows within fracture planes until fracture intersections are encountered. For example, for a fracture plane with a dip of 81° , the horizontal distance at a vertical distance of 21.1 m from the liquid release point is 3.3 m. This kind of water-diversion mechanism can be handled in the current model (based on the continuum approach) only by using the strong heterogeneity of rock properties in the lateral direction. The large k_f calibrated for Column 13 facilitates the lateral water flow from the central columns. The calibrated α_f for Column 13 is twice as large as that for the central rock columns, but the capillary force (caused mainly by the fracture-saturation difference between the surrounding rock mass and the central columns) diverts more water away from the central area.

In summary, the calibrated fracture permeability in the upper unit reflects the spatial variability in the measured infiltration rates, and is consistent with the air-permeability data in terms of the geometric mean and standard deviation.

4.1.2. Correlation between Measured Infiltration Rate and Fracture Density

Figure 9 shows the spatial variability in normalized infiltration rates for the first 90 days and the later 125 days. The normalized infiltration rate for a subplot was obtained by dividing the mean (measured) infiltration rate of this subplot averaged over the first 90 days of high infiltration (or the later 125 days of low infiltration) by the mean total infiltration rate during the same period. Strong spatial variability can be observed in Figure 9: Subplot 2 with the highest normalized infiltration rates accounts for about 30% of the total infiltration rates at both early and later times, whereas Subplot 4 with the

smallest normalized infiltration rate accounts for only 1.5%; the sum of the normalized infiltration rates in six subplots (Subplots 1, 2, 9, 10, 11, and 12) is 83% of the total infiltration rates. This spatial variability can be attributed to the (spatially varying) characteristics of network of actively-water-conducting fractures, which may be a fraction of globally connected fractures in the unsaturated flow system. The globally connected fractures and actively-water-conducting fractures are not known for the system. However, the discrete fracture patterns mapped on the infiltration plot were used to explore the correlation between fracture density and measured infiltration rates.

Figure 10 shows the positive correlation between normalized infiltration rates and fracture density. The fracture density for a subplot was calculated using total fracture trace length surveyed over the surface area of the subplot (Bear et al., 1993). A number of fractures intersect the infiltration plot, allowing for infiltration through the fractures (see Figure 2). The fracture density varies from zero to 4.03 m^{-1} (in Subplot 11), with an average value of 1.31 m^{-1} (over 12 subplots). Four different cases for the relation between measured infiltration rates and fracture density are evaluated for the 12 subplots.

In the first case, generally low infiltration (for Subplots 4, 6, and 8) occurred because no fractures longer than 1.0 m were involved (with zero fracture density) or only a very short segment of a large fracture was involved (with a very small fracture density). The low infiltration rates occurred through small fractures, which are not included in the fracture map. Infiltration rates were relatively stable since the first-day high infiltration that may have been result of the large water-storage capacity of small fractures and cavities and the imbibition of unsaturated matrix in the rock beneath the subplots.

In the second case, the measured infiltration rate is relatively low and stable with time, although one or two large fractures intersect Subplots 3, 5 and 7, leading to a fracture density close to the mean. The infiltration series in these subplots, similar to those in the first case, imply that the mapped fractures (or fracture segments) within these subplots may not be globally connected, or may not actively conduct water flow.

In the third case, the relatively high infiltration rates measured in Subplots 1, 2, 10, and 11 may stem from generally large fracture density in these subplots. For example, four fractures intersect Subplot 11, leading to the highest fracture density. One or two

large fractures pass through the other three subplots (Subplots 1, 2, and 10), leading to fracture density close to its mean value. However, these fractures extend out of the infiltration plot, which may allow for in-fracture-plane flow diversion into areas out of the infiltration plot (Dahan et al., 1999). The four subplots also share a similar three-stage pattern for infiltration rates, which is similar to that of the total infiltration rate (see Figure 4). The infiltration rate in Subplot 2 is high at both early and later time, because the infiltrated water may flow within a well-connected fracture network. For Subplots 1, 10, and 11, the infiltration rate is high at early time but low at later time, because some water-conducting fractures active at early time may fail in conducting water at later time (Doughty, 2000; Faybishenko et al., 2003).

In the final case, substantial and stable infiltration rates occurred in Subplots 9 and 12, possibly because of relatively large fracture density and a well-connected fracture network. Large fractures intersect these subplots and extend out of the infiltration plot area. Fracture mapping also indicates that there are a very large number of small fractures (not included in the fracture map) around the two subplots. These large and small fractures may enhance fracture connectivity in the fractured rock under these two subplots. This enhanced connectivity produced stable infiltration rates over the entire test period, with little dynamic behavior.

The correlation between normalized infiltration rates and fracture density is weakened by in-fracture-plane heterogeneity. This heterogeneity may stem from (1) the spatially varying distributions of hydraulic apertures, (2) the connectivity of fractures underlying the infiltration plot, and (3) conditions of in-fill materials within fractures (Wealthall et al., 2001). For example, for the single fracture passing through Subplots 2, 5, and 9, the infiltration rates for the fracture segments within these three subplots are very different, indicating flow focusing in small segments of the fracture. The spatial variability of infiltration rates along single fractures indicates that the in-plane heterogeneity plays a critical role in controlling water percolation. This is consistent with the findings observed by Dahan et al. (1999) in a single fracture, through which only 50% of the open fracture segments allowed significant flow, and less than 20% of the fracture opening transmitted high flow rates.

The correlation between normalized infiltration rates and fracture density is different for the early time of high infiltration and the later time of low infiltration. The normalized infiltration rate is more sensitive to the calculated fracture density at early time than at later time (see Figure 10), as shown by the correlation at early time (with a correlation coefficient of 0.59) stronger than that at later time (with 0.32). The different correlations may result from the different dynamic behavior of infiltration rates in different subplots (see Figure 4), as well as the transient nature of total infiltration rates (see Figure 3). As shown in Figure 9, the normalized infiltration rates (the relative contribution to the total infiltration rate) remain stable during both time periods in a number of subplots (i.e., Subplots 2–8). In the other subplots (i.e., Subplots 1 and 9–12), however, significant change in the normalized infiltration rates was observed from early to later time. For example, Subplots 1, 10, and 11 account for 44% of the total infiltration rate at early time, whereas they produce much less infiltration (23%) at later time. The infiltration rate in Subplot 12 increases its percentage from 8% at early time to 20% at later time.

For the transient nature of infiltration rates (for Subplots 1, 2, 10, and 11, and the entire infiltration plot), the reduction over time in infiltration rates may primarily result from the failure of water-conducting fractures (and active portions of fractures) to transmit water (Faybishenko et al., 2003). The internal fracture connectivity is complicated: some fractures may not connect with other fractures, while others are connected to each other; only a fraction of all fractures are globally connected. The fracture connectivity (which affects infiltration) is also related to the scale of water percolation. Infiltrated water through the infiltration plot flows downward along fractures. Once the dead ends of fractures are reached, the infiltrated water fills in the dead-end fractures, and these fractures no longer contribute to infiltration. We refer to this situation as a failure of the fractures in conducting infiltrated water. The failure of water-conducting fractures is time-dependent. As the infiltration process proceeds, initially-conducting-water fractures may no longer conduct water (because they are not globally connected), leading to fewer fractures conducting water flow and a decrease in infiltration rates. Meanwhile, the infiltrated water moves downward, and fracture connectivity becomes more important to unsaturated flow and to the infiltration process.

The fracture-failure mechanism affects the transient infiltration series, but it may not participate in the quasi-steady-state flow regime at later time. At later steady-state time, the infiltrated water flows through active globally connected fractures, and the infiltration rates tend to be stable. Note that the above discussion focuses on the infiltration rates since the 30th day, because the complex transient nature within the first 30 days was affected by many other factors, such as dynamic movement of in-fill materials, and discharge and dissolution of entrapped air. The above interpretation is consistent with the findings obtained by a numerical model for a field infiltration test, Idaho (Doughty, 2000). In her model, the tributary structure of fracture pattern was explicitly considered with the matrix block. This model reproduced the general trend of decreasing infiltration rate, which is representative of a funneling of flow (Faybishenko et al., 2000).

In summary, the positive correlation between measured infiltration rates and fracture density indicates that discrete fractures in the infiltration plot play a critical role in water percolation, especially in the early-time flow behavior. The measured infiltration rates reflect the effects from the total actively water-conducting fractures (and fracture segments), while the fracture density calculated using the fracture map on the alcove floor does not distinguish active fractures (segments) from inactive ones. In addition, in-fracture-plane heterogeneity and complicated dynamic effects weaken such correlations, indicating that capturing the discrete features of a fracture network does not mean fully capturing the complicated unsaturated flow.

4.1.3. Correlation between Calibrated Permeability and Fracture Density

Figure 11 shows a positive correlation between calibrated $\log k_f$ and fracture density. This correlation demonstrates that the calibrated fracture permeability partially captures the spatially varying discrete fractures within the infiltration plot. The largest calibrated fracture permeability in Rock Column 11 corresponds to the highest calculated fracture density in Subplot 11. However, the correlation is not very strong, with a correlation coefficient of 0.55. This positive but not strong correlation indicates the importance of focusing flow (resulting from in-fracture-plane heterogeneity) in single fractures (Dahan et al., 1999; Salve et al., 2004), and of the connectivity of actively-water-conducting fractures in fracture networks (Liu et al., 1998; Glass et al., 2002). The

calibrated fracture permeability also includes contributions from small fractures, because non-zero infiltration rates were observed for subplots with zero fracture density observed (without considering small fractures). *The calibrated fracture permeability is believed to represent the actively participating fractures (or fracture segments), which are reflected in the measured infiltration rates.*

4.2. Correlations in the Lower Unit

Unlike correlations for the upper unit, the mutual correlations for the lower unit, among the calibrated fracture properties, measured seepage rates, and fracture patterns on the niche ceiling, are quite complicated, because the measured seepage rates reflect all unsaturated flow processes within the fracture network and water-diversion mechanisms around the niche.

4.2.1. Correlation between Calibrated Rock Properties and Measured Seepage Rate

We used the normalized seepage rate for the correlation analysis. The normalized seepage rate for a tray unit was obtained by dividing the mean seepage rate averaged over the early 90 days (or later 125 days) in the tray unit, by the maximum mean seepage rate during the same time period. Figure 12 shows the spatial variability of the normalized seepage rate at early and later times.

Figure 13a shows that calibrated $\log \alpha_f$ is negatively correlated with normalized seepage rate at later time, with a correlation coefficient of -0.46. The calibrated α_f varies over 1.5 orders of magnitude in space, with $\log \alpha_f$ ranging from -3.62 to -2.27 Pa^{-1} . The mean and standard deviation are $\log \alpha_f = -2.97 \pm 0.45$. The spatial variability in the calibrated α_f in the lower unit corresponds well to that of the normalized seepage rate. In the x direction (see Figure 7), the relative α_f values over several rock columns can be interpreted by the normalized seepage rates. For example, the calibrated α_f values for Columns 3–6 in the first tray unit row demonstrate that a smaller α_f value (higher capillary strength) corresponds to a higher seepage rate. The measured seepage rate in Tray Unit 6 is the highest among the four columns, and the calibrated α_f for Column 6 is

the lowest. The same situation is true for Columns 9–12 (Columns 11 and 12 share the same normalized seepage rates in Tray Unit 11). The lowest α_f value was obtained for Column 12, where the highest seepage rate was measured in the second row of tray units. Note that the correlation is stronger at later time than at early time, because of the higher weight factor used in the objective function for the later seepage data, and the quasi-stable features of measured seepage rates at later time.

Figure 13b shows that the calibrated $\log k_f$ value in the lower unit is well correlated to the normalized seepage rate at later time, with a correlation coefficient of -0.70 . Large calibrated k_f values occur at Columns 1, 2, 7, and 8, where the seepage rates through their corresponding tray units are relatively low. For example, the calibrated k_f for Column 1 is $2.25 \times 10^{-12} \text{ m}^2$ (the second largest), while the seepage rate at early and later times is the lowest. On the other hand, the calibrated k_f for rock columns with high seepage rates at both early and later times is low. For example, the calibrated k_f for Column 12 is $1.43 \times 10^{-14} \text{ m}^2$, but its seepage rate is the second highest at both early and later times. The calibrated k_f varies over three orders of magnitude for the 13 rock columns, ranging from 1.89×10^{-15} to $4.34 \times 10^{-12} \text{ m}^2$. This range is similar to that of the measured air permeability, which ranges from 1.43×10^{-15} to $6.22 \times 10^{-12} \text{ m}^2$. The mean calibrated $\log k_f$ is -13.38 , which is close to that of \log air permeability (-13.40).

The negative correlations between calibrated rock properties (α_f and k_f) and normalized seepage rates seem to contradict the concept that water in fractured rocks flows along preferential flow paths (e.g., large fractures or faults) with high permeability or apertures. However, the calibrated rock property results are understandable in the framework of the numerical modeling in the following two aspects. First, we can use water balance for a rock column subsystem in the lower unit to understand the negative correlation between calibrated $\log \alpha_f$ and normalized seepage rates. The inflow to the subsystem from its top boundary is the vertical flux at the contact between the upper and lower units. The net inflow to this subsystem may also be through the side boundaries of

this subsystem. At the later time, the transient effects are small, and the total net inflow into this subsystem is approximately identical to the outflow (seepage) rate at the niche ceiling. When the inflow rate on the top boundary is smaller than the measured seepage rate, inflow through the side boundaries from neighboring subsystems is needed to make up the difference. This side-boundary inflow is driven primarily by capillary pressure gradients, which is related to the heterogeneity of α_f . For a subsystem with a large normalized seepage rate, a α_f value smaller than its neighboring rock columns may be needed to imbibe water from its neighbors, resulting in the negative correlation. Secondly, the strong negative correlation between calibrated $\log k_f$ and normalized seepage rate may stem from the following considerations: the calibrated k_f values for rock columns with significant seepage rates depend mainly on the measured travel times of wetting fronts. In the numerical model, both vertical and horizontal connections were used for fracture and matrix continua, with some fracture-matrix connections. Because unsaturated flow is gravity-dominant, the simulated flux and travel time depend mainly on the calibrated k_f . In the field, wetting-front travel times were affected by many factors, such as the complex connectivity of water-conducting fractures. For example, fractures, which are not globally connected, contributed to early infiltration, but did not contribute to seepage; these fractures retarded the arrival of the wetting fronts and increased their travel times. However, such factors were not captured in the current continuum-approach numerical model. As a result, the k_f values calibrated using the measured travel times represent the lumped effects from all affecting factors. The calibrated rock properties within the framework of the numerical model may not be the real physical rock properties; instead, they are model-related parameters, which are used to match the measured infiltration/seepage rates in the simplified model.

Linear regression indicates that calibrated $\log k_f$ is very weakly correlated with calibrated $\log \alpha_f$ (a correlation coefficient of 0.14), as assumed in model calibration, in spite of both rock parameters being correlated to the normalized seepage rates at later time. This lack of correlation may not affect the calibration results, because a weaker correlation between k_f and α_f in fracture networks than in porous media is expected,

and the capillary strength in fracture networks is much smaller than in porous media (Zhou et al., 2002).

4.2.2. Correlation between Measured Seepage Rate and Fracture Density

Figure 14 shows the correlations between normalized seepage rates (at early high-infiltration and later low-infiltration times) and fracture density on the niche ceiling. The fracture density was calculated for each tray unit using natural fractures (longer than 1.0 m) on the fracture map shown in Figure 5. The fracture density was obtained by dividing the total fracture trace length surveyed by the surface area of the tray unit. No correlation was found for the early-time seepage rates, and a weakly negative correlation was found for the later-time seepage rates. This lack of correlation may be attributed to the complicated unsaturated flow in the fracture network and flow diversion in the vicinity of Niche 3.

Flow in the fracture network transited from saturated flow in the upper portion of the system to complex unsaturated flow under conditions of low percolation rates in the lower portion of the system, particularly in the vicinity of the niche. The unsaturated flow in the lower portion of the system was complicated by many factors. First, seepage drips into the niche through fractures, because of dominant fracture flow and little matrix flow in the lower unit. Second, in-fracture-plane heterogeneity leads to fragmented and fingered flow within single fractures. Such a flow may not be a function of fracture trace length represented by fracture density. Flow fragmentation and fingers are major features of unsaturated flow in fractured rock under low-flow-rate conditions (Glass et al., 2002). Finally, the mapped fractures on the niche ceiling may be globally connected, but the global unsaturated flow may occur only in a fraction of the connected fractures, as indicated by the active fracture model (Liu et al., 1998). *The lack of correlation demonstrates the importance of fragmented and fingering flow within single fractures, and of active fractures in a fracture network.*

The lack of correlation between normalized seepage rate and calculated fracture density also demonstrates the importance of water diversion around the niche caused by (1) small fractures and excavation-induced fractures, (2) capillary-barrier-layer effects, and (3) film flow on the niche ceiling. First, small fractures and excavation-induced

fractures may be connected with water-conducting fractures above the niche. For example, water in a water-conducting fracture, which ends at a distance above the ceiling, may be redistributed (or diverged) into such connected small fractures, and may disperse on the niche ceiling. In addition, small fractures may imbibe water at fracture intersections from large fractures, because the small fractures have higher capillarity than the large fractures. The excavation of the niche induced many fractures around the niche ceiling, enhancing fracture connectivity in different directions and facilitating flow diversion. Secondly, capillarity is a very important mechanism for water diversion around the niche ceiling (Philip, 1990; Finsterle, 2000). A capillary barrier layer may exist above the niche ceiling, because of the zero-capillarity boundary condition on the ceiling and sidewall of Niche 3. Within the capillary layer, flow can redistribute among all connected fractures, leading to weaker correlation between the normalized seepage rate and the calculated density of large fractures. Finally, water flow leaving from fractures may flow around the niche ceiling in the form of film flow (Tokunaga and Wan, 1997). The film flow may be caused by surface roughness and the geometric shape of the niche ceiling. This type of flow was observed in seepage tests in other niches at Yucca Mountain by Trautz and Wang (2002).

4.2.3. Potential Flow Path Clusters

Two potential flow-path clusters can be identified using (1) the transient patterns of measured seepage rates in different tray units (see Figures 6 and 12), and (2) the fracture maps on the alcove floor and the niche ceiling (see Figures 2 and 5). Each cluster may contain a number of flow paths, which may vary with time. The measured seepage rates in the first row of tray units (i.e., Tray Units 1–6) exhibit transient patterns different from those in the second row (i.e., Tray Units 7–11) in the early time between the 30th and 90th day. In the second row, the seepage rate dropped very quickly after seepage occurred approximately on the 30th day. In the first row, however, seepage rate increased after the first occurrence of seepage on the 32nd day, and the seepage rate reached its peak on the 60th day. In each row, the measured seepage rates share very similar transient patterns among different tray units. The similar-in-row but different-between-rows feature may imply that two flow-path clusters exist for the unsaturated flow. In

addition, the normalized seepage rates in the two rows of tray units also exhibit different behavior at early and later time, as shown in Figure 12. Normalized-seepage-rate distribution in the first row is similar for both early and later times. However, such a distribution for the second row changes dramatically from early time to later time.

The two flow-path clusters can also be identified using the fracture maps on the niche ceiling and alcove floor. Four large fractures intersect the seepage capture system and pass through both the first and second row of tray units. It seems that fracture segments intersected in the first row contribute to the first cluster, while the segments in the second row contribute to the second cluster. The difference in the seepage rates in the two clusters may result primarily from the difference in infiltration on the alcove floor. Water flow in the first cluster may stem from high infiltration in Subplot 2 and its neighboring subplots. The large fracture intersected by Subplot 2 may be hydraulically connected with fractures (on the niche ceiling) intersecting with Tray Units 2 and 3. The second cluster may connect segments of the four fractures in the second row to large fractures in Subplot 11 and its neighbors, through which infiltrated water exhibits an earlier infiltration peak (on the 15th day) than in the first cluster.

The two flow-path clusters exhibit different correlations between the normalized seepage rates and fracture density. At early time, infiltration was high, resulting in a high flow rate and less focused flow within fractures. For the first cluster, a positive correlation was found, with a correlation coefficient of 0.49. In this cluster, high seepage rate corresponds to high fracture density. For example, Tray Unit 3, intersecting three large fractures, has relatively high seepage rates, whereas Tray Unit 4 has a shorter fracture trace length and lower seepage rates. A weaker correlation (with a correlation coefficient of 0.27) was obtained for the second cluster, indicating that seepage is more complex for the second cluster. Tray Unit 11 has the second highest seepage rate, while its fracture density is relatively small, indicating that the high seepage rate may focus within a short fracture trace length. At later time, no correlation was obtained between seepage rates and fracture density for either flow-path cluster, because fragmented flow and fingers may occur within single fractures. Evidence of fragmented and fingered flow can be seen in the seepage through the two fractures intersecting Tray Units 2, 3, 7, and 8. The fracture segments in the first cluster continued to contribute to substantial seepage,

while those in the second cluster carried little flow, resulting in very small, intermittent seepage. However, at early time, all fracture segments of the two fractures were active in conducting seepage. *This demonstrates that more fragmented and fingered flow occurs under low-flow-rate conditions, leading to weak correlation between seepage rates and fracture density. Under higher-infiltration conditions, the unsaturated flow is more pervasive and the correlation is higher.*

4.3. Evaluation of the Continuum Approach

Figure 15 shows the match between the measured total seepage rate for the entire niche and the simulated total seepage rate using calibrated rock properties. The match is good for the entire test period, in particular for the later time. The very good match at later time may result from the high weight factor used for the later-time seepage rates in the objective function of Equation (7). The quasi-stable nature of seepage and infiltration rates at later time also helps produce good matches. During the early time between the 30th and 90th day, the match is also reasonable. The simulated maximum seepage rate is close to the measured one. No stable stage of 30 days in the calibrated seepage series was obtained, while a stable high seepage rate occurred in the measured seepage series. The stable stage in the measured seepage rate resulted from a combination of increasing seepage rate in the first flow-path cluster and decreasing seepage rate in the second cluster.

The simulated seepage occurs on the 20th day, earlier than the measured seepage, which occurred on the 30th day since liquid release. The difference in the wetting-front travel times can be explained by the handling of different kinds of data in the objective function of Equation (7). In model calibration, a large weight factor ($\omega_1 + \omega_4$) was used to force seepage not to occur within the first 20 days, while a smaller weight factor (ω_1) was used for the misfit between the measured and calibrated seepage rates between the 20th and 30th day, allowing for the occurrence of seepage during this period. The reason for doing this was that many retardation factors (e.g., dynamic connectivity of water-conducting fractures) affecting the wetting-front travel time could not be considered in the current continuum-approach numerical model. The high degree of uncertainty in initial matrix saturation values used in the model may also affect the travel time, because

the matrix imbibes water flowing in fractures into the matrix, delaying the arrival of the wetting front at the niche ceiling. If a period of firm 30 days for no-seepage occurrence was used, the calibrated fracture permeability would be too small to be reasonable for the test site.

Figure 16 shows the match between calibrated and measured seepage series associated with the 12 rock columns in the lower unit. The match is generally good in terms of the time-dependent seepage series. Simulated and measured seepage rates for Column 12 are close to each other. For Column 7, for example, significant differences between simulated and measured seepage rate were obtained between the 30th and 90th day, but a good match was obtained for the later time, with low seepage rates. Again, this may result from the high weight factor used for the misfit of later-time seepage rates, and the strong dynamic effects in the measured seepage rates. For some columns, measured seepage rates decline with time faster than simulated ones at later time, because of the many dynamic effects of fragmented unsaturated flow in fractured rock.

The good match for the total seepage rates indicates that the continuum approach can simulate complex unsaturated flow in the mesoscale test system. The good match for seepage rates for each of the 12 tray units also demonstrates that the calibrated heterogeneity in fracture capillary strength and permeability can be used to reproduce the spatial variability in the measured seepage rates. Measured infiltration and seepage rates are indicative of the lumped effects of complicated fracture connectivity, flow interaction between fractures and matrix, and active fractures and fracture segments. The calibrated rock properties for the continuum approach reflect the lumped effects of various factors on unsaturated flow, and are representative of actively participating fractures in the fracture network and active segments within individual fractures.

5. Conclusions

A mesoscale field test was conducted for investigating large-scale unsaturated flow (including infiltration and seepage) in deep, fractured rock. Water was injected into an infiltration plot on the floor of an alcove, and seepage was collected from the ceiling of a niche located directly under the infiltration plot. A number of infiltration subplots and seepage collection tray units were used to investigate spatial variabilities in both

infiltration and seepage series. A three-dimensional unsaturated flow model was developed and calibrated to match the spatial variabilities. The fracture permeability and van Genuchten α_f were calibrated for each of rock columns, which correspond to the configuration of seepage collection tray units in the lower hydrogeologic unit or the infiltration subplots in the upper hydrogeologic unit. Correlation analysis was conducted for calibrated rock properties, measured infiltration and seepage rates, and discrete fractures mapped on the alcove floor and niche ceiling, in terms of large fractures and fracture density. We conclude the following:

- With the aid of column-based heterogeneity, the calibrated numerical model is able to match seepage data in terms of seepage occurrence and rates measured. The good match between the measured and simulated total seepage rates indicates that the continuum approach is applicable for tracking mesoscale unsaturated flow in fractured rock.
- Significant water diversion measured in the field test, caused by fracture orientations in the discrete fracture network, can be captured in the numerical model, by the strong heterogeneity of capillary force strength and of fracture permeability in the lateral direction.
- The calibrated rock properties in both the upper and the lower hydrogeologic units correlate well with the measured infiltration and seepage rates, which reflect lumped features of small-scale flow processes.
- The positive correlation between measured infiltration rates and fracture density on the alcove floor demonstrates that infiltration under ponding conditions are controlled by discrete fractures on the infiltration plot. But other factors, such as in-fracture-plane heterogeneity and dynamic connectivity of water-conducting fractures, also play an important role in complicating the infiltration processes. Such factors, along with induced temporal variabilities, can be captured by model calibration using the continuum approach.
- The lack of correlation between measured seepage rates and fracture density on the niche ceiling indicates the importance of actively-water-conducting individual

fractures and active segments of individual fractures, as well as water diversion around the niche caused by a combination of different mechanisms.

Acknowledgments

We thank Diana Swantek (LBNL) for her contributions in the preparation of graphics for this paper. We thank Paul Cook for thorough internal technical reviews, and Dan Hawkes for improving the quality of this paper with his editorial comments. Thanks are also due to Stefan Finsterle for his help in using the parallel version of iTOUGH2. This work has been supported by the Director, Office of Civilian Radioactive Waste Management, U.S. Department of Energy, through Memorandum Purchase Order EA9013MC5X between Bechtel SAIC Company, LLC and the Ernest Orlando Lawrence Berkeley National Laboratory (Berkeley Lab). The support is provided to Berkeley Lab through the U.S. Department of Energy Contract No. DE-AC03-76SF00098.

References

- Bear, J., Tsang, C.-F., and de Marsily, G. (eds.), 1993. Flow and contaminant transport in fractured rock. Academic Press, Inc., San Diego.
- Bodvarsson, G.S., and Tsang, Y. (Guest Editors), 1999. Yucca Mountain Project. *J. Contam. Hydrol.* 38, 1–146.
- Bodvarsson, G.S., Ho, C.K., and Robinson, B.A. (Editors), 2003. Yucca Mountain Project. *J. Contam. Hydrol.* 62-63, p750.
- Brown, S., Caprihan, A., and Hardy, R., 1998. Experimental observation of fluid flow channels in a single fracture. *J. Geophys. Res.* 103, 5125–5132.
- BSC (Bechtel SAIC Company), 2003a. In Situ Field Testing of Processes. ANL-NBS-HS-000005 REV02B, Bechtel SAIC Company, Las Vegas, Nevada.
- BSC, 2003b. Calibrated Properties Model. MDL-NBS-HS-000003 REV 01, Bechtel SAIC Company, Las Vegas, Nevada.
- BSC, 2003c. Analysis of Hydrologic Properties Data. MDL-NBS-HS-000014 REV 00, Bechtel SAIC Company, Las Vegas, Nevada.
- Buesch, D.C., and Spengler, R.W., 1998. Character of middle nonlithophysal zone of the Topopah Spring Tuff at Yucca Mountain, in Proceedings of the Eighth International Conference on High-Level Radioactive Waste Management. 11-14 May, 592–593, Am. Nucl. Soc., Las Vegas, NV.
- Cacas, M.C., Ledoux, E., de Marsily, G., Barbreau, A., Calmels, P., Gaillard, B., Margritta, R., 1990. Modeling fracture flow with a stochastic discrete fracture network: Calibration and validation, 2, The transport model. *Water Resour. Res.* 26, 491-500.
- Cook, P., 2000. In situ pneumatic testing at Yucca Mountain. *Int. J. Rock Mech. Min. Sci.* 37, 357–367.
- Dahan, O., Nativ, R., Adar, E.M., Berkowitz, B., and Ronen, Z., 1999. Field observation of flow in a fracture intersecting unsaturated chalk. *Water Resour. Res.* 35(11), 3315–3326.
- Doughty, C., 1999. Investigation of conceptual and numerical approaches for evaluating moisture, gas, chemical, and heat transport in fractured unsaturated rock. *J. Contam. Hydrol.* 38, 69–106.
- Doughty, C., 2000. Numerical model of water flow in a fractured basalt vadose zone: Box Canyon site Idaho. *Water Resour. Res.* 36(12), 3521–3534.
- Doughty, C., Salve, R., Wang, J.S.Y., 2002. Liquid-release tests in unsaturated fractured welded tuffs: II. Numerical modeling. *J. Hydrol.* 256, 80–105.
- Dverstorp, B., Andersson, J., and Nordqvist, W., 1992. Discrete fracture network interpretation of field tracer migration in sparsely fractured rock. *Water Resour. Res.* 28(9), 2327–2343.
- Fabryka-Martin, J.T., Dixon, P.R., Levy, S.S., Liu, B., Brenner, D.L., Wolfsberg, L.E., Turin, H.J., and Sharma, P., 1996. Implications of environmental isotopes for flow and transport in the unsaturated zone at Yucca Mountain, Nevada. *Geol. Soc. Am. Abstr. Programs*, 28(7), A-414.

- Faybishenko, B., Doughty, C., Steiger, M., Long, J.C.S., Wood, T.R., Jacobsen, J.S., Lore, J., and Zawislanski, P.T., 2000. Conceptual model of the geometry and physics of water flow in a fractured basalt vadose zone. *Water Resour. Res.* 36(12), 3499–3520.
- Faybishenko, B., Bodvarsson, G.S., and Salve, R., 2003. On the physics of unstable infiltration, seepage, and gravity drainage in partially saturated tuffs. *J. Contam. Hydrol.* 62–63, 63–87.
- Finsterle, S., 1999. iTOUGH2 user's guide. Report LBNL-40040, UC-400, Lawrence Berkeley National Laboratory, Berkeley, CA.
- Finsterle, S., 2000. Using the continuum approach to model unsaturated flow in fractured rock. *Water Resour. Res.* 36(8), 2055–2066.
- Finsterle, S., Ahlers, C.F., Trautz, R.C., and Cook, P.J., 2003. Inverse and predictive modeling of seepage into underground openings. *J. Contam. Hydrol.* 62–63, 89–109.
- Flint, L.E., 1998a. Matrix properties of hydrogeologic units at Yucca Mountain, Nevada. U.S. Geological Survey Open-File Report, MOL.19970324.0046, U.S. Geological Survey, Denver, CO.
- Flint, L.E., 1998b. Characterization of hydrogeologic units using matrix properties, Yucca Mountain, Nevada. USGS Water resources investigation report 97-4243, Denver, CO.
- Glass, R.J., Nicholl, M.J., and Tidwell, V.C., 1995. Challenging models for flow in unsaturated, fractured rock through exploration of small scale flow processes. *Geophys. Res. Lett.* 22(11), 1457–1460.
- Glass R.J., Nicholl, M.J., Ramirez, A.L., and Daily, W.D., 2002. Liquid phase structure within an unsaturated fracture network beneath a surface infiltration event: field experiment. *Water Resour. Res.* 38(10), 1199, doi:10.1029/2001WR000167
- Hinds, J.J., Bodvarsson, G.S., and Nieder-Westermann, G.H., 2003. Conceptual evaluation of the potential role of fractures in unsaturated processes at Yucca Mountain. *J. Contam. Hydrol.* 62–63, 111–132.
- Liu, B., Fabryka-Martin, J., Wolfsberg, A., Robinson, B., and Sharma, P., 1995. Significance in apparent discrepancies in water ages derived from atmospheric radionuclides at Yucca Mountain, Nevada. Rep. LA-UR-95-572, Los Alamos Natl. Lab., Los Alamos, NM.
- Liu, H.H., Doughty, C., Bodvarsson, G.S., 1998. An active fracture model for unsaturated flow and transport in fractured rocks. *Water Resour. Res.* 34(10), 2633–2646.
- Liu, H.H., Bodvarsson, G.S., and Finsterle, S., 2002. A note on unsaturated flow in two-dimensional fracture networks. *Water Resour. Res.* 38(9), 1176, doi:10.1029/2001WR000977.
- Liu H.H., Zhang, G., and Bodvarsson, G.S., 2003a. The active fracture model: its relation to fractal flow patterns and an evaluation using field observations. *Vadose Zone J.* 2: 259–269.

- Liu, H.H., Haukwa, C.B., Ahlers, C.F., Bodvarsson, G.S., Flint, A.L., and Guertal, W.B., 2003b. Modeling flow and transport in unsaturated fractured rock: an evaluation of the continuum approach. *J. Contam. Hydrol.* 62–63, 173–188.
- Liu, H.H., Salve, R., Wang, J.S.Y., and Hudson, D., 2004. Field investigation into unsaturated flow and transport in a fault: 3. model analysis. *J. Contam. Hydrol.* (in press).
- Nativ, R., Adar, E., Dahan, O., and Geyh, M., 1995. Water recharge and solute transport through the vadose zone of fractured chalk under desert conditions. *Water Resour. Res.* 31(2), 253–261.
- Neuman, S.P., 1994. Generalized scaling of permeabilities: validation and effect of support scale. *Geophysical Research Letters*, 21(5), 349–352.
- Nicholl, M.J., Glass, R.J., and Wheatcraft, S.W., 1994. Gravity-driven infiltration instability in initially dry nonhorizontal fractures. *Water Resour. Res.* 30(9), 2533–2546.
- NRC (National Research Council), 2001. Conceptual models of flow and transport in the fractured vadose zone. National Academy Press, Washington D.C.
- Ohman, J., and Niemi, A., 2003. Upscaling of fracture hydraulics by means of an oriented correlated stochastic continuum model. *Water Resour. Res.* 39(10), 1277, doi:10.1029/2002WR001776.
- Philip, J.R., 1990. Some general results on the seepage exclusion problem. *Water Resour. Res.* 26(3), 367–377.
- Pruess, K., and Narasimhan, T.N., 1985. A practical method for modeling fluid and heat flow in fractured porous media. *Soc. Pet. Eng. J.* 25, 14–26.
- Pruess, K., 1999. A mechanistic model for water seepage through thick unsaturated zones in fractured rocks of low matrix permeability, *Water Resour. Res.* 35(4), 1039–1051.
- Pruess, K., Oldenburg, C.M., and Moridis, G., 1999. TOUGH2 user's guide. Report LBNL-43134, Lawrence Berkeley National Laboratory, Berkeley, CA.
- Richards, L.H., 1931. Capillary conduction of liquids through porous mediums. *Physics* 1, 318–333.
- Salve, R., Oldenburg, C.M., and Wang, J.S.Y., 2003. Fault-matrix interactions in nonwelded tuff of the Paintbrush Group at Yucca Mountain. *J. Contam. Hydrol.* 62–63, 269–286.
- Salve, R., Liu, H.H., Hu, Q., Hudson, D., Cook, P., and Czarnomski, A., 2004. Unsaturated flow and transport through a fault embedded in fractured welded tuff. *Water Resour. Res.* 40(4), W04210, doi:10.1029/2003WR002571.
- Su, G.W., Geller, J.T., Pruess, K., and Wen, F., 1999. Experimental studies of water seepage and intermittent flow in unsaturated, rough-walled fractures. *Water Resour. Res.* 35(4), 1019–1037.
- Therrien R., and Sudicky, E.A., 1996. Three-dimensional analysis of variably-saturated flow and solute transport in discretely-fractured porous media. *J. Contam. Hydrol.* 23, 1–44.

- Tokunaga, T.K., and Wan, J., 1997. Water film flow along fracture surfaces of porous rock. *Water Resour. Res.* 33(6), 1287–1295.
- Trautz R.C., and Wang, J.S.Y., 2002. Seepage into an underground opening constructed in unsaturated fractured rock under evaporative conditions. *Water Resour. Res.* 38(10), 1188, doi:10.1029/2001WR000690.
- van Genuchten, M.T., 1980. A closed-form equation for predicting the hydraulic conductivity of unsaturated soils. *Soil Sci. Soc. Am. J.* 44, 892-898.
- Wang, J.S.Y., and Bodvarsson, G.S., 2003. Evolution of the unsaturated zone testing at Yucca Mountain. *J. Contam. Hydrol.* 62–63, 337–360.
- Wang, J.S.Y. and Elsworth, D., 1999. Permeability Changes Induced by Excavation in Fractured Tuff. *Rock Mechanics for Industry, Proceedings of the 37th U.S. Rock Mechanics Symposium*, Vail, Colorado, USA, 6-9 June 1999. Amadei, B.; Kranz, R.L.; Scott, G.A.; and Smeallie, P.H., eds. 2, 751-757. Brookfield, Vermont: A.A. Balkema.
- Warren, J.E., and Root, P.J, 1963. The behavior of naturally fractured reservoirs. *Soc. Pet. Eng. J.* 245-255, *Transactions, AIME*, 228.
- Wealthall, G.P., Steele, A., Bloomfield, J.P., Moss, R.H., and Lerner, D.N., 2001. Sediment filled fractures in the Permo-Triassic sandstones of the Cheshire Basin: observations and implications for pollutant transport. *J. Contam. Hydrol.* 50, 41–51.
- Wu, Y.S., Ritcey, A.C., and Bodvarsson, G.S., 1999. A modeling study of perched water phenomena in the unsaturated zone at Yucca Mountain. *J. Contam. Hydrol.* 38, 157-184.
- Yang, I.C., Rattay, G.W., and Yu, P., 1996. Interpretation of chemical and isotopic data from boreholes in the unsaturated zone at Yucca Mountain, Nevada. *U.S. Geol. Surv. Water Resour. Invst. Rep.*, 96-4058, 58 pp.
- Zhou, Q., Gelhar, L.W., Jacobs, B., 2002. Comparison of field-scale effective properties of two-phase flow in heterogeneous porous media obtained by stochastic analysis and numerical experiments. In Findikakis A.N. (Ed.), *Proceedings of the international groundwater symposium on bridging the gap between measurements and modeling in heterogeneous media*, Berkeley, California.
- Zhou, Q., Liu, H.H., Bodvarsson, G.S., and Oldenburg, C.M., 2003. Flow and transport in unsaturated fractured rock: effects of multiscale heterogeneity of hydrogeologic properties. *J. Contam. Hydrol.* 60, 1–30.
- Zhou, Q., Birkholzer, J.T., Javandel, I., and Jordan, P.D., 2004. Modeling three-dimensional groundwater flow and advective contaminant transport at a heterogeneous mountainous site in support of remediation. *Vadose Zone J.* (in press).

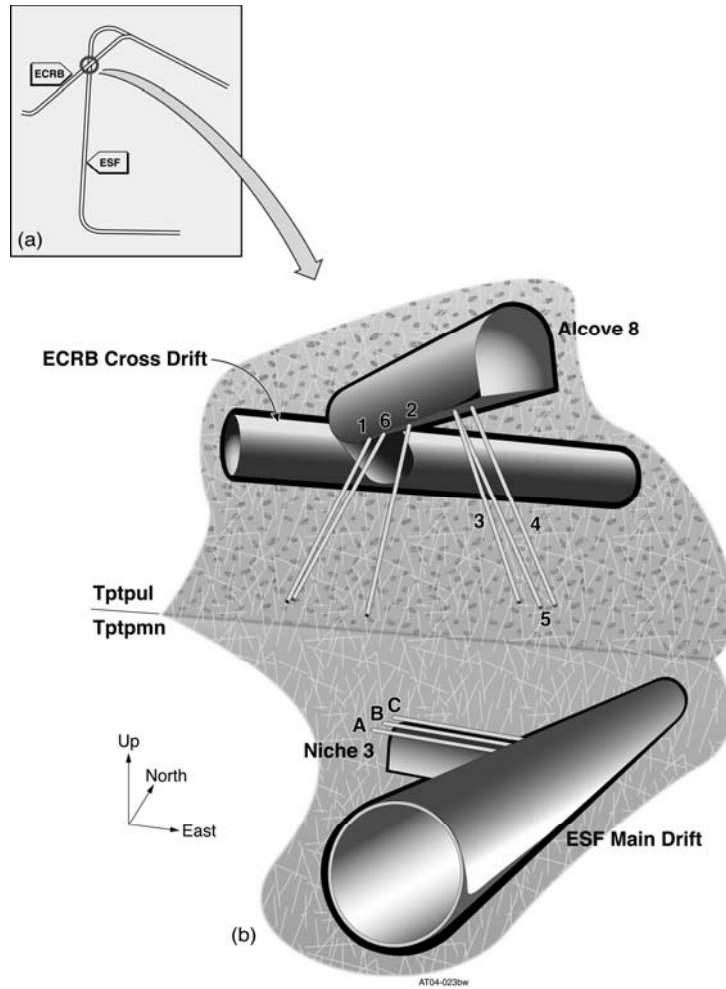


Figure 1. (a) Crossover point of the ESRB Main Drift and ECRB Cross Drift, and (b) schematic illustration of the test bed for the infiltration and seepage test in the Alcove 8–Niche 3 system, with six near-vertical boreholes around Alcove 8 and three horizontal boreholes above the ceiling of Niche 3.

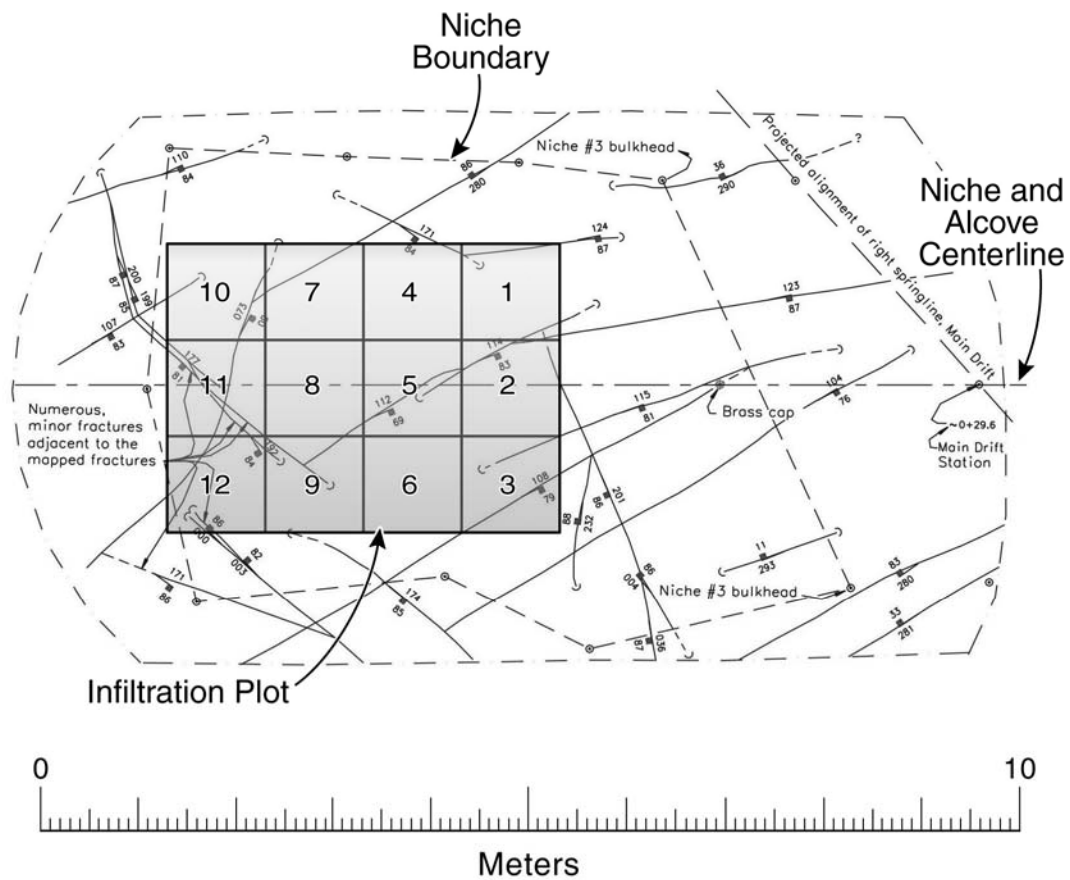


Figure 2. Fracture map on the floor of Alcove 8 with configuration of the 12 infiltration subplots used for the test.

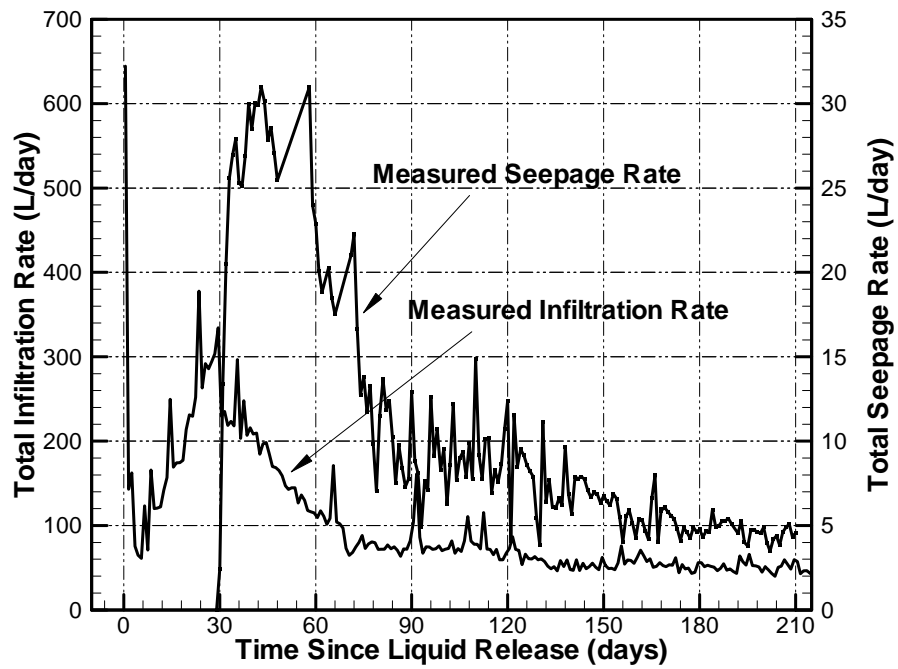


Figure 3. Total infiltration rate (L/day) measured through the infiltration plot and total seepage rate (L/day) measured through the ceiling of Niche 3.

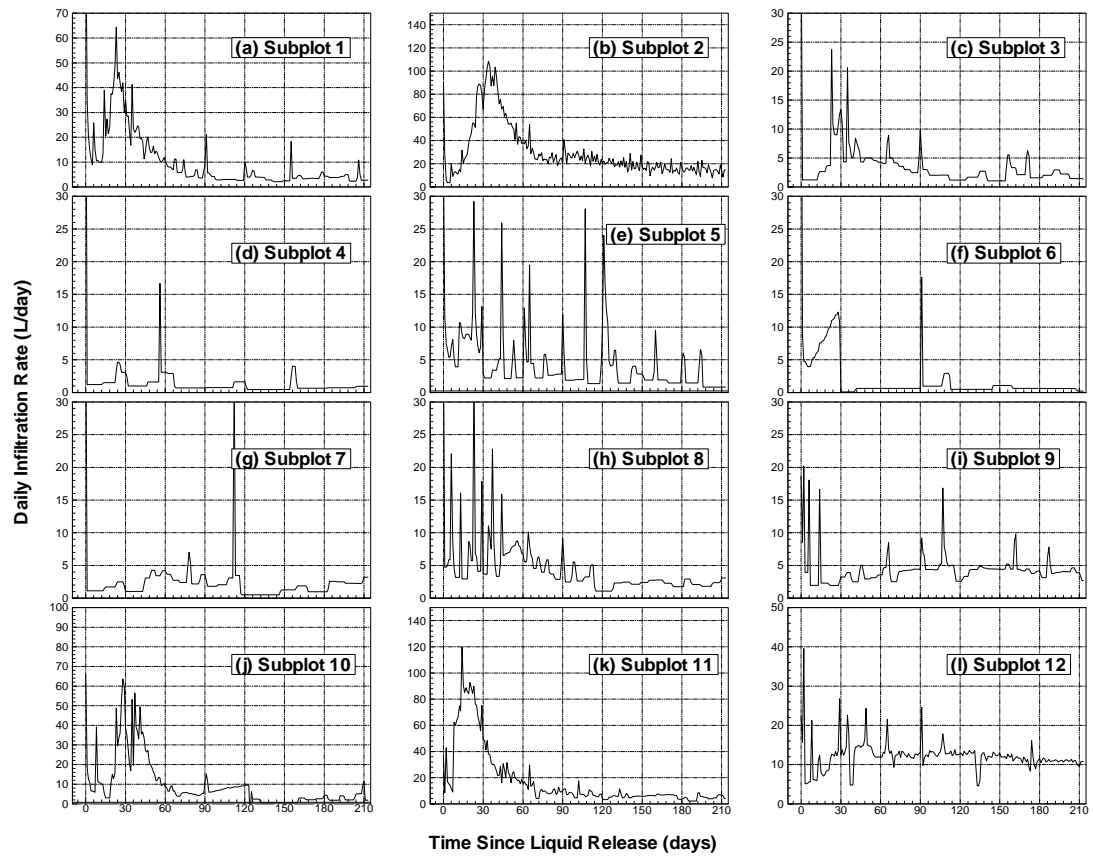


Figure 4. Time series of infiltration rates (L/day) measured at the 12 infiltration subplots located on the floor of Alcove 8.

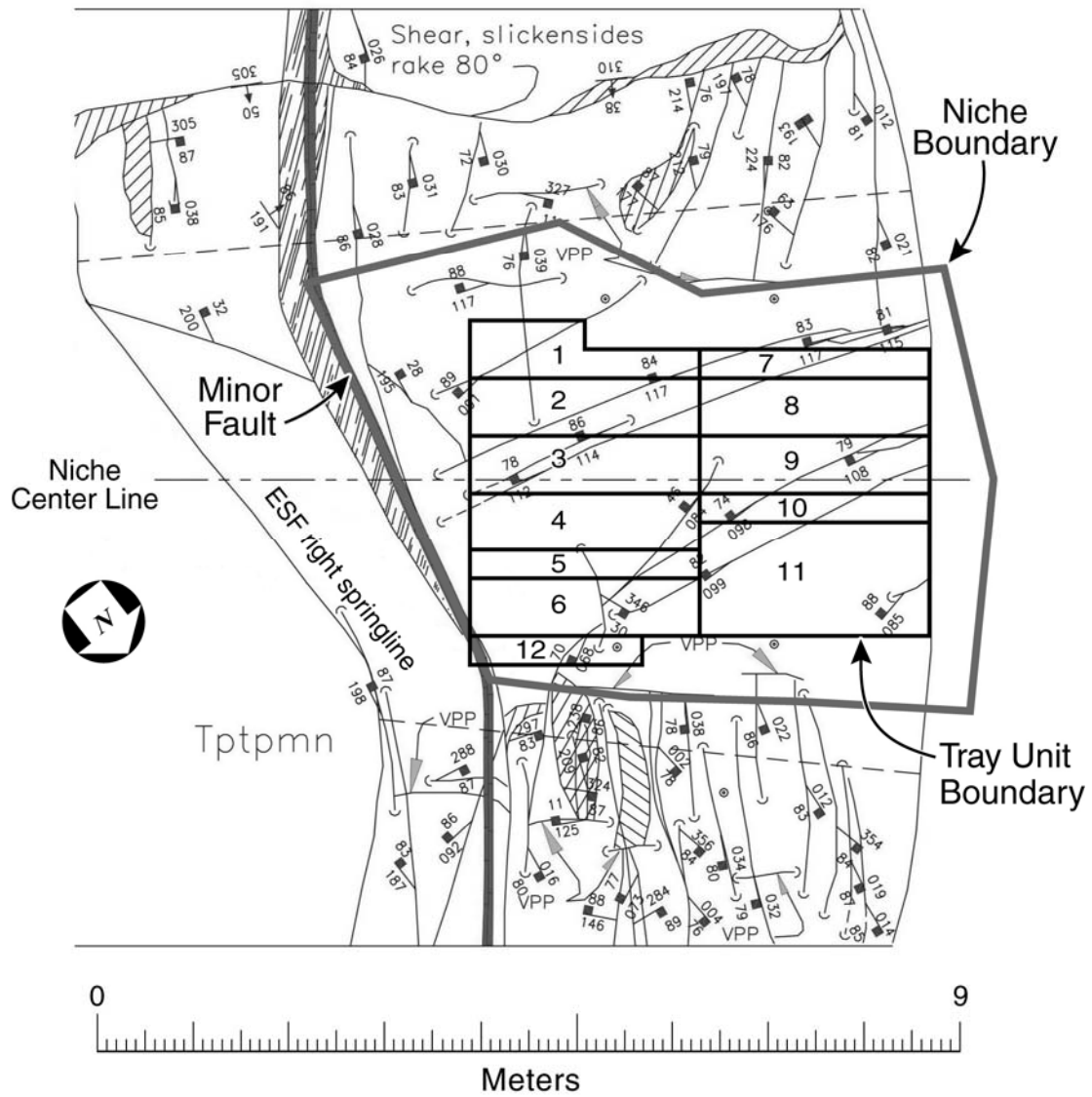


Figure 5. Fracture map on the ceiling and sidewalls of Niche 3, and boundary of the niche floor and configuration of 12 tray units of the seepage capture system.

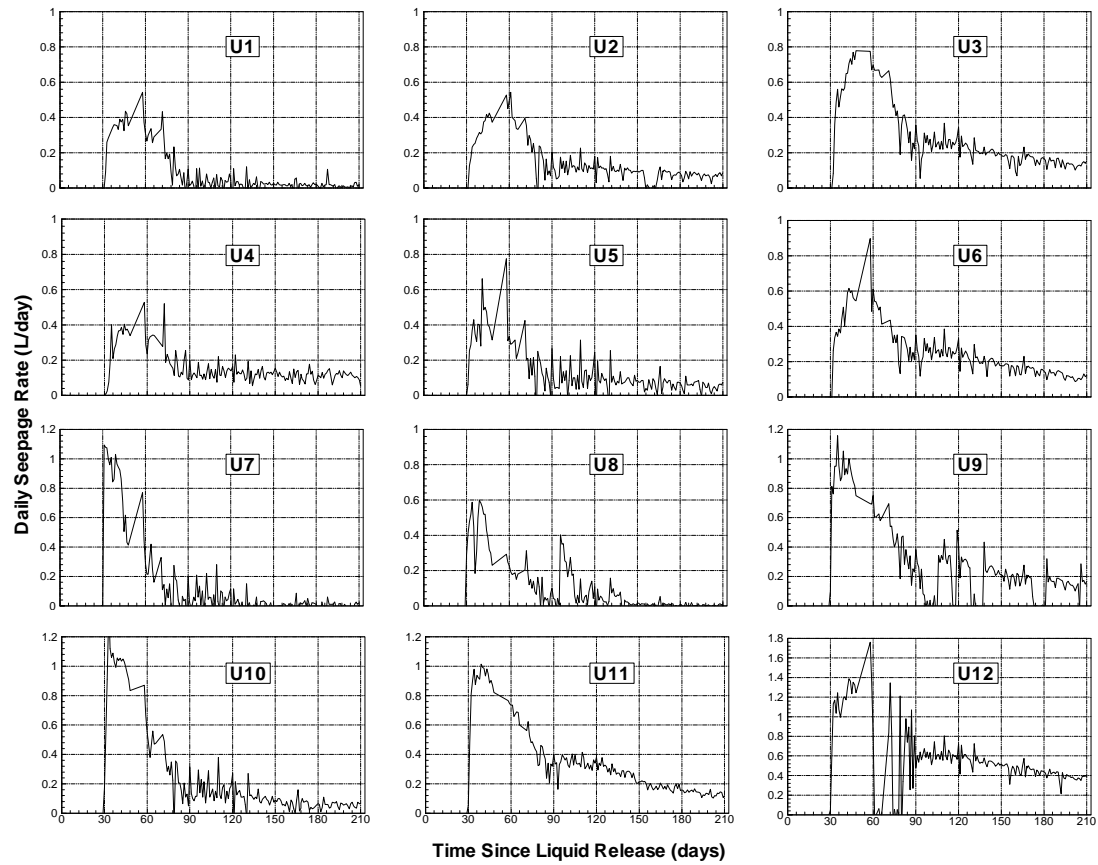


Figure 6. Transient seepage rates (L/day), per unit area of a subtray (0.3 m by 1.2 m), measured for the 12 tray units at the ceiling of Niche 3

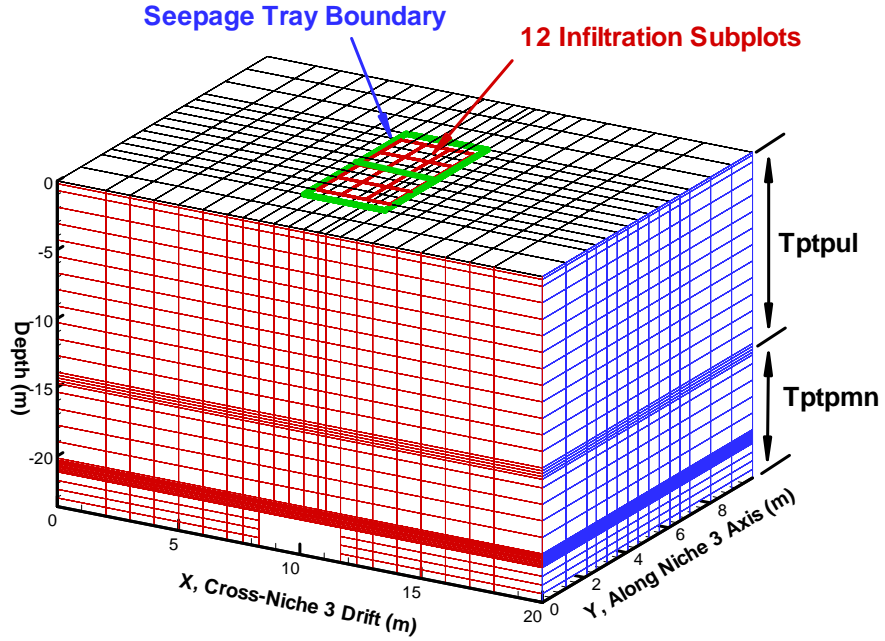


Figure 7. Study domain and the three-dimensional numerical grid used for the model calibration for the infiltration and seepage test.

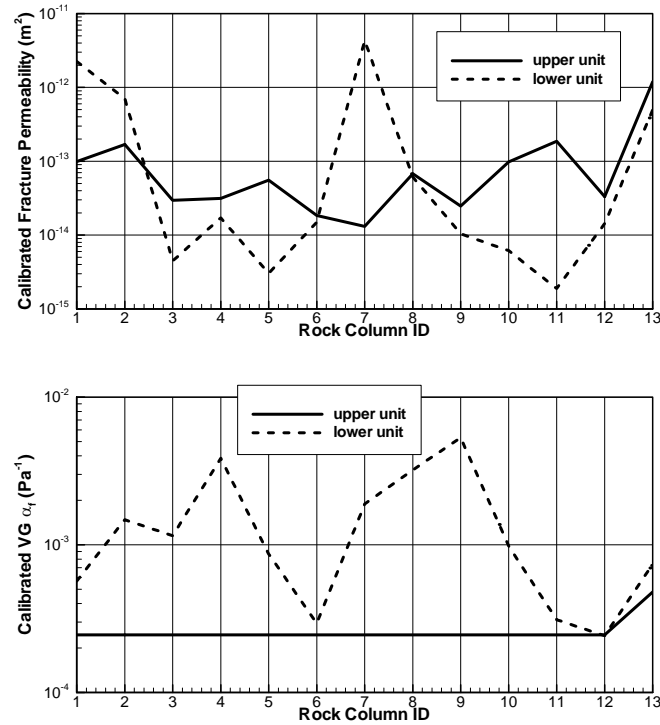


Figure 8. Calibrated fracture permeability and VG α_f for the upper and lower hydrogeologic units.

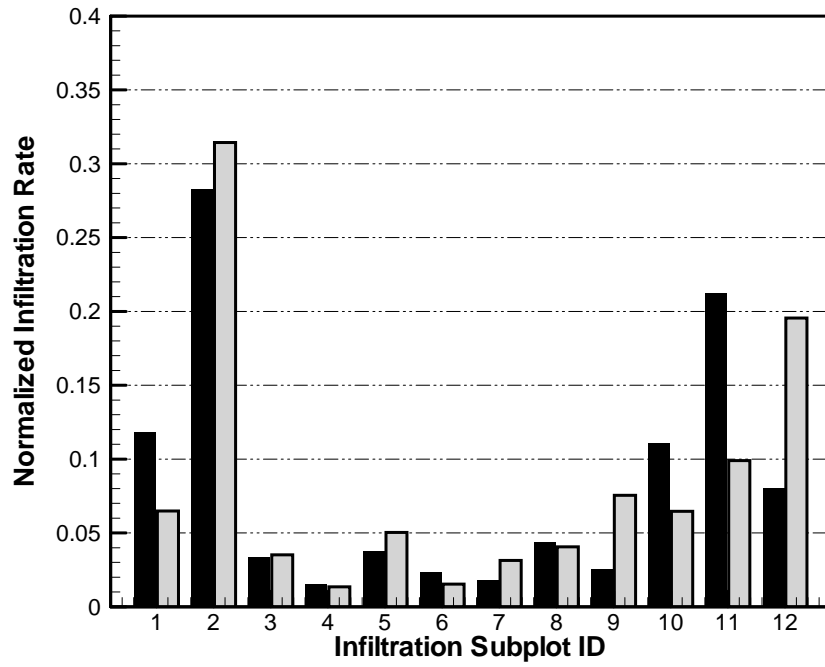


Figure 9. Spatial variability of normalized infiltration rates measured for the 12 subplots for the first 90 days (black histogram) and for the later 125 days (gray histogram).

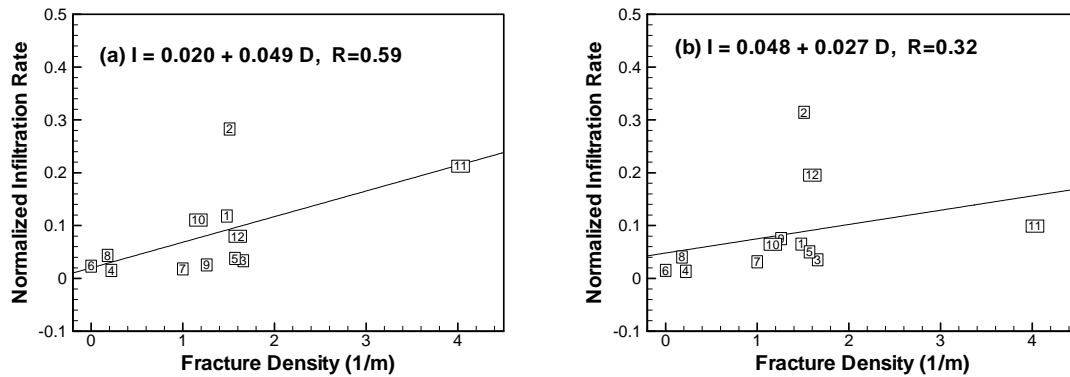


Figure 10. Correlation between the normalized (measured) infiltration rates (I) for (a) the first 90 days and (b) the later 125 days, and fractures density (D) calculated for each infiltration subplot at the floor of Alcove 8. Note that R is the correlation coefficient.

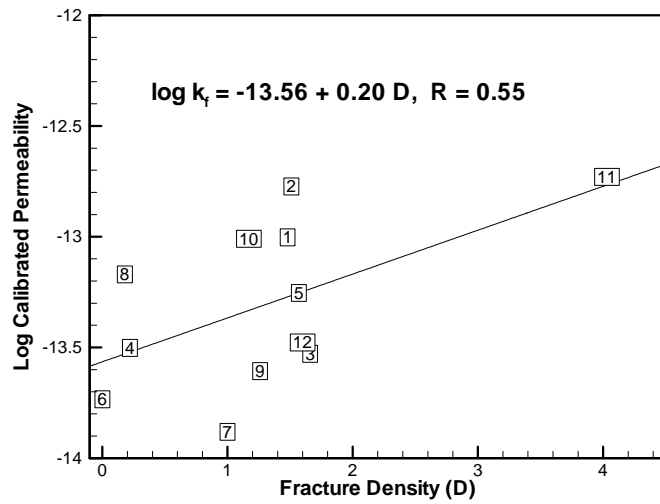


Figure 11. Correlation between calibrated fracture permeability (m^2) for the upper hydrogeologic unit and fracture density (m^{-1}) on the alcove floor.

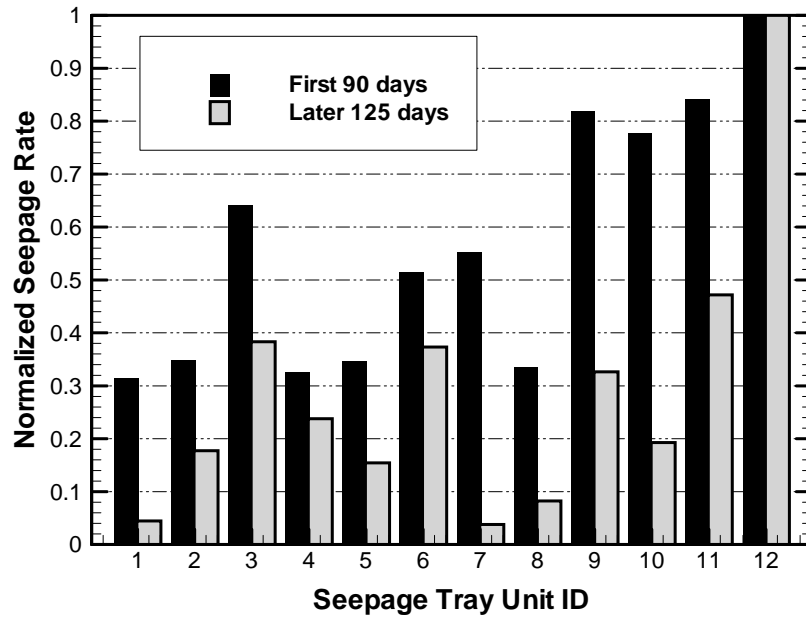


Figure 12. Spatial variability of the normalized seepage rates for the first 90 days and the later 125 days.

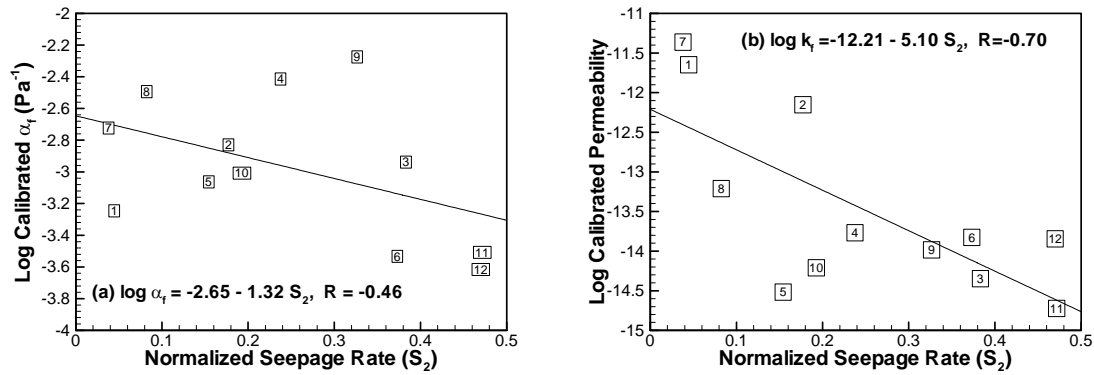


Figure 13. Correlations between the normalized seepage rates for the later time and (a) calibrated fracture α_f and (b) calibrated fracture permeability.

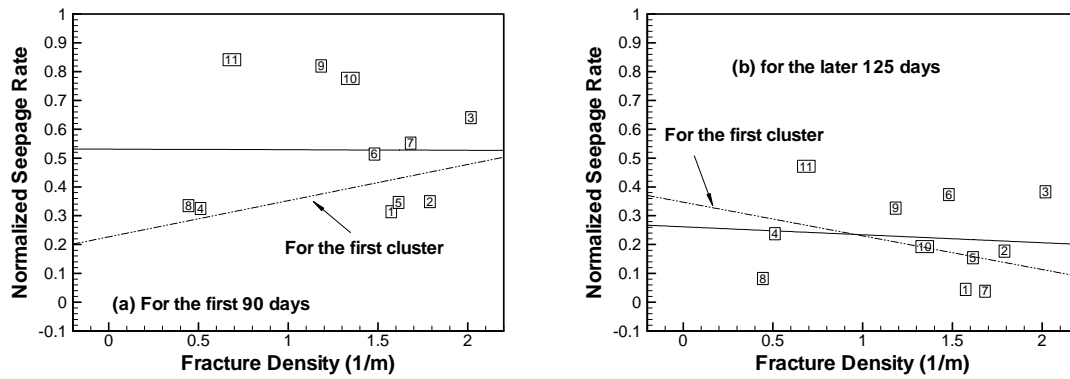


Figure 14. Correlations between the normalized seepage rates and fracture density calculated for the 12 tray units at the ceiling of Niche 3. Shown are also the correlations for the first flow-path cluster.

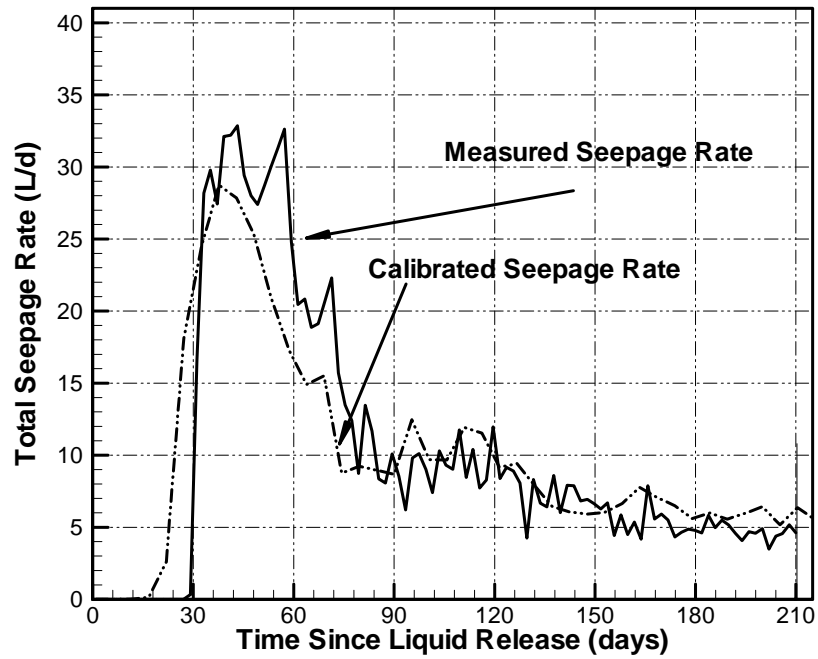


Figure 15. Match between the measured total seepage rate series and the simulated series using calibrated rock properties.

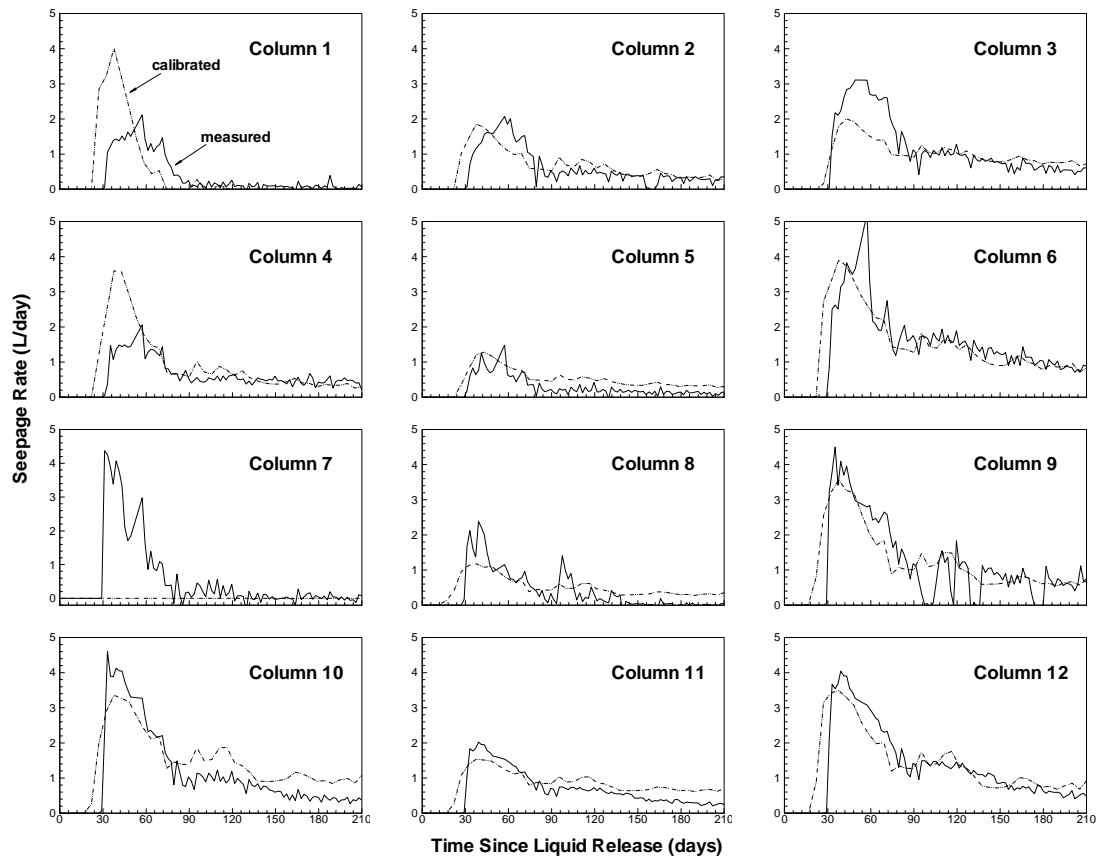


Figure 16. Matches between measured seepage rates (solid lines) and simulated seepage rates (dash-dot-dot lines) using calibrated rock properties for 12 seepage rock columns.